Universiteit Utrecht

Opleiding Natuur- en Sterrenkunde

Coupling artificial atoms: a detailed investigation of the accessible parameter space

Bachelor Thesis

Sam Borman

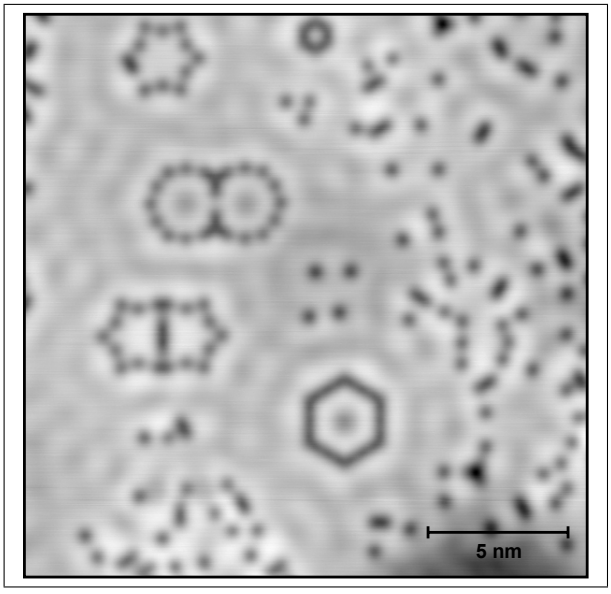

Supervisors:

Dr. Ingmar Swart Supervisor
Condensed Matter & Interfaces

Saoirsé Freeney, MSc. Daily supervisor
Condensed Matter & Interfaces

16-01-2019

Abstract

Artificial atoms can be created by confining the surface state electrons of a metal in a configuration of repulsive scatterers adsorbed onto that metal, effectively creating a particle in a box. Here a scanning tunneling microscope was used to arrange carbon monoxide molecules into hexagonal shapes on Cu(111). The differential conductance was measured, giving an indication for the on-site energy of these artificial atoms. For varying sizes a relation $E \propto \frac{1}{A}$ was confirmed, as expected from a particle in a box. When coupled together into dimeric and trimeric shapes the artificial atoms show behavior expected from the theory of tight binding. This gives an indication for the experimentally accessible parameter space (ϵ, t and s) under different configurations of CO on Cu(111). Furthermore, the work function profile of CO on Cu(111) was mapped, showing a decrease in work function when the STM tip was above the molecule. These results can be used as a basis for building larger artificial structures.

The title image shows a 20 x 20 nm overview scan of several of the artificial atoms that have been built. The scan was taken at a bias voltage of 0.100 V and a current setpoint of 30 pA. Three individual atoms of edge lengths $2a$, $4a$ and $6a$ are seen, the latter two of which have been blocked from the environment with additional CO molecules. In the middle two dimers with blocked edges of length $4a$ and $5a$ can be seen. The barrier in the middle of these dimers features additional CO molecules with the goal of decoupling the atoms.

Contents

1 Introduction

"What would happen if we could arrange the atoms one by one the way we want them [...]"[1]. With this famous question posed in his classic talk *There's plenty of room at the bottom* from 1959, Richard Feynman invited scientists from all over the globe to enter a new field of physics; the field of nanophysics. Though at that time it seemed like an idea very far away, Feynman's question was soon responded to with the invention of the scanning tunneling microscope (STM) by Gerd Binnig and Heinrich Roher in 1981. The STM can not only be used to image surfaces at the atomic level but it is even capable of manipulating individual atoms. This was first done by Eigler and Schweizer, spelling out the IBM logo with Xenon atoms in 1990[2], thus granting access to this whole new field of physics that Feynman postulated 30 years earlier.

With this revolutionary technique it became possible to build structures atom by atom that are otherwise unknown to nature. In particular it is possible to manipulate carbon monoxide absorbed on a material with a well defined surface state, like Cu(111). The CO molecules act as a repulsive scatterer for the surface state electrons[3]. By manually positioning the CO molecules it is possible to confine this 2D electron gas, creating a particle-in-a-box situation. We call this confined 2DEG an artificial atom due to the similar behavior of the electrons as when bound to an atomic nucleus.

Multiple of these artificial atoms can be coupled, creating a lattice. This has already been done with for example honeycomb[4], Lieb[5], Sierpinski[6] and Penrose tiling[7] structures. To aid in the interpretation of experimental results, tight binding calculations are performed. Relevant parameters such as the coupling strength, i.e. the the hopping parameter, t, and orbital overlap, s, are adjusted such that the theoretically calculated density of states matches the experimental values. It as been found that next-nearest-neighbor coupling is often essential to obtain good agreement with experimental data[5][6].

Theoretical models of these lattices were tuned to the experiment with hopping parameters t in the range 0.06 to 0.15 eV and orbital overlap s ranging from 0.02 to 0.2[5][6]. It is unknown however, to what extend these parameters can be varied, i.e. it is unclear if we can experimentally access the theoretically predicted features of these artificial lattices.

In this thesis I will look into the experimentally accessible parameter space, i.e. what values ϵ, t and s can have, depending on the configuration of the CO molecules. This will be done by building several artificial atoms of varying size and coupling them in various ways. Furthermore I will look into some properties of carbon monoxide in the STM. In particular I will measure the work function of the STM tip when it's above CO and compare it to its value above bare Cu(111), 4.98 eV [8]. I will then move the CO molecules closer together to see how the work function changes when 2 CO molecules are influencing each other.

2 Theoretical background

2.1 Scanning Tunneling Microscopy

Scanning tunneling microscopy uses the effect of quantum tunneling to characterize surfaces on an atomic scale. An atomically sharp tip is brought close to the sample surface. When the electron wavefunctions of the tip and sample overlap, a finite tunneling conductance is generated. By applying a bias voltage V between the tip and the sample a current can run. If $V > 0$ the electrons will be tunneling from the occupied states of the tip into the empty states of the sample. For $V < 0$ the electrons will tunnel from the sample to the tip[9].

A general overview of a scanning tunneling microscope is shown in figure 1. The movement of the tip over the sample is controlled by both a coarse motor made out of piezoelectric crystals and a fine piezo scanner. Depending on the type of STM the coarse motor either controls the movement of the sample or of the tip. The fine piezo always controls the movement of the tip. Piezoelectric crystals can expand and contract depending on the applied voltage, enabling them to move the tip in atomically small steps. The coarse motor is used to move the tip in larger steps.

The tip can approach the sample with the coarse motor at first but as it gets closer to the surface an auto-approach should be started to prevent accidentally crashing into the surface. The auto-approach extends the fine piezo towards the surface until a set tunneling current is measured, the current setpoint. If the fine piezo reaches its maximum extension without measuring that current it retracts again and the motor does a coarse step. This process continues until the current setpoint is reached. This way of auto-approaching ensures that the tip does not crash into the surface when bringing it in tunneling contact.

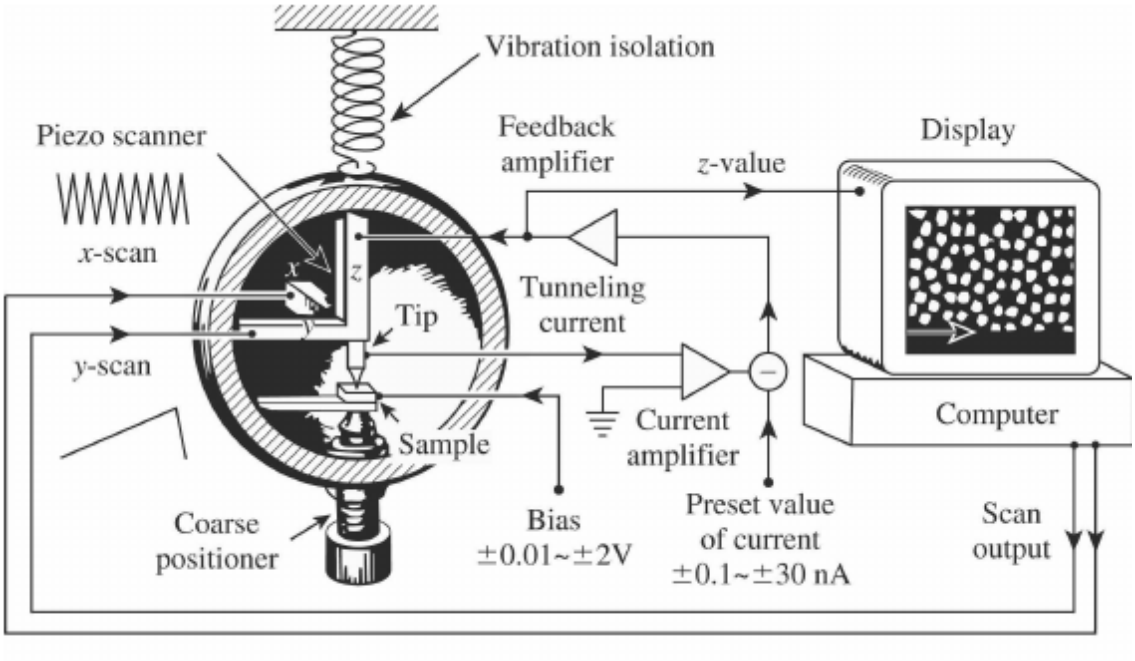

Figure 1: Schematic overview of a scanning tunneling microscope. Image taken from Julian Chen, C. 2008. *Introduction to Scanning Tunneling Microscopy*[9].

The tunneling current is proportional to the tunneling probability which in turn is exponentially sensitive to the tunneling distance according to the WKB approximation[8]. This leads to the proportionality

$$I \propto e^{-2\frac{\sqrt{2m\phi}}{\hbar}z}, \tag{1}$$

where I is the tunneling current, m the electron mass, ϕ the effective barrier height for tunneling and z the distance between the tip and sample[8].

A current amplifier is used to convert the tunnel current into a voltage which can be compared the current setpoint. The difference with this reference value is used to drive the fine piezo in the z-direction in negative feedback, ensuring a current of the setpoint is always maintained. This is called "feedback loop". In this feedback mode, the tip is set to scan over the surface using its fine piezo in the x- and y-direction. Due to variations of height in the surface a different tunneling current will be detected which then drives the tip up or down. The height change of the tip can be recorded on a computer which leads to an atomically precise contour plot of the sample surface.

Because we require the tip to move over the sample with atomic precision it is important to isolate the microscope stage from any external vibrations. To achieve this the stage is suspended on several springs that can compensate for vibrations. Other precautions can be taken to reduce the vibrations but those shall be discussed in section 3.

2.2 Atom manipulation

The STM is not only capable of making an atomically sharp image of a sample surface but the tip is also capable of manipulating atoms or molecules adsorbed on the surface. Moving atoms is done by placing the tip above the desired atom and gradually increasing the current setpoint. This leads to the tip moving closer to the atom and as a result a partial chemical bond between tip and atom is formed [9]. When the strength of this bond matches a certain barrier energy, i.e. the binding between the atom and the sample surface, moving the tip sideways should move the atom in the same direction. When the atom is at the desired location the current setpoint is decreased such that the bond between tip and atom breaks, leaving the atom behind at its new position.

2.3 Scanning Tunneling Spectroscopy

Scanning tunneling spectroscopy can be used to measure the local density of states (LDOS) as a function of electron energy. By placing the tip at the desired location and fixing its height the electron current, I, and the differential conductance, dI/dV, can be measured as a function of electron energy by varying the bias voltage[10].

An adsorbate on the surface, i.e. a molecule, atom or even an artificial atom, functions as a barrier tunneling junction. At a certain positive bias the Fermi levels of the tip and of the unoccupied orbitals of the adsorbate will align and electrons from the tip will be able to tunnel into the orbitals. At a sufficient negative bias, electrons will tunnel into the tip from the occupied states of the adsorbate which will be replenished by electrons from the sample substrate [10].

It can be shown[9] that in the Bardeen transfer Hamiltonian method for low temperatures and constant tunneling matrix element the tunnel current will reduce to

$$I \propto \int_0^{eV} \rho_S(E_F - eV + \epsilon)\rho_T(E_F + \epsilon)d\epsilon, \tag{2}$$

where ρ_S and ρ_T are the density of states in the sample and the tip respectively. Under the assumption that ρ_T is constant, differentiating 2 to the bias V gives

$$\frac{dI}{dV} \propto \rho_S(E_F - eV). \tag{3}$$

This shows that in order to obtain information on the occupancy of different energy levels the differential tunneling conductance has to be measured.

2.4 Electronic structure of a Cu(111) surface

Many metals, including Cu(111), feature a so called surface state. Surface state electrons have a wavefunction that peaks at the surface of the metal and exponentially decays in the direction normal to the surface[8]. These states are thus confined to the surface and behave as a two dimensional electron gas (2DEG). Cu(111) features a surface state at an energy of -0.45 eV [6].

Another material property to consider in STM experiments is the work function. The work function is defined as the potential energy difference between the vacuum and the Fermi level of said metal [8].The work function is given by

$$W = -\epsilon_F + W_s, \tag{4}$$

where ϵ_F is the Fermi level and W_s is the work needed to carry electrons through an additional electric field that arises from certain deficiencies [11]. In STM the work function is generally equal to the effective barrier height ϕ from equation 1. The work function above a Cu(111) surface is 4.98 eV [8].

2.5 Confining the surface state

An artificial atom can be created by confining the surface state electrons from a two dimensional electron gas (2DEG) in between repulsive scatterers. This technique was pioneered by Crommie et al who used Iron adatoms on a Cu(111) surface to build a quantum corral [12]. However, many more repulsive scatterers can be used to confine this two dimensional electron gas to a certain geometry, in particular carbon monoxide molecules (CO)[4].

Figure 2a) shows the geometric structure of Cu(111). CO molecules adsorb directly on top of the copper atoms, so we can only place them along the geometry of Cu(111). In the STM however the CO molecules show up with a radius $r_{CO} \approx 0.3$ nm, larger than the Cu(111) nearest neighbor distance $a = 0.255$ nm. In figure 2b) an STM scan of CO on Cu(111) is shown. The wavelike pattern around the CO molecules shows us that they scatter the surface state electrons.

Interestingly, when imaged with a metal tip, CO shows up as a dip in STM images, meaning that the tip has to get closer to the surface in order to maintain its current setpoint above a CO molecule. DFT calculations suggest that it could be due to an interference effect between the wave functions of the tip and the sample surface above a CO [13].

It is experimentally clear however that CO acts as a repulsive scatterer for the surface state electrons, making it a perfect candidate to build artificial structures with. In particular, confining the 2DEG to the geometry of a lattice creates said lattice of artificial atoms. This technique has been used to create for example Lieb[5], Sierpinski[6] and honeycomb[4] geometries. Measuring the local density of states at the different sites of these lattices shows good agreement with muffin-tin and tight binding calculations.

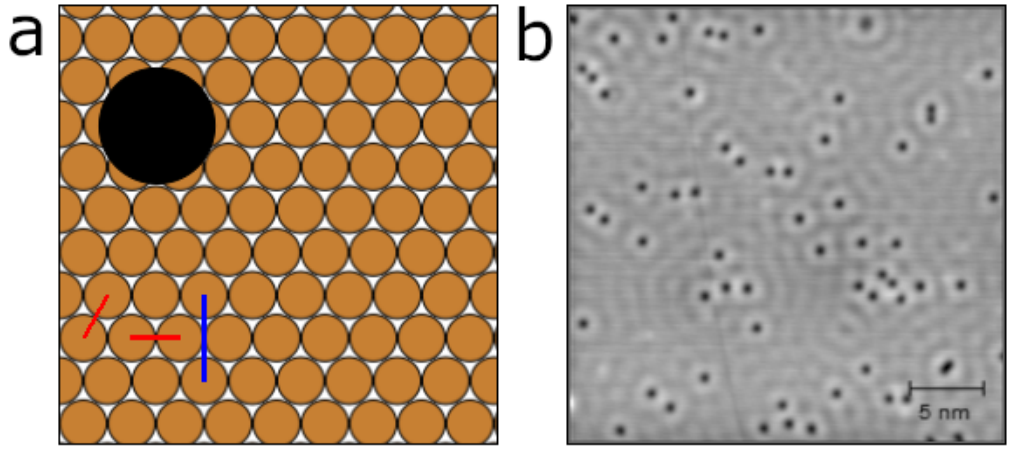

Figure 2: **a** The geometric structure of Cu(111) is shown. A CO molecule adsorbs directly on top of a copper atom but appears with a radius $r_{CO} = 0.3$nm in the STM. The red bar shows the nearest neighbor distance, $a = 0.255$ nm, of Cu(111). The blue bar shows the next nearest neighbor distance $\sqrt{3}a$. **b.** Scan at bias 0.100 V and I-setpoint 30 pA showing the scattering of the surface state around adsorbed CO molecules.

2.6 The tight-binding model

In solid state physics the tight-binding model provides a means to calculate the electronic band structure of a lattice. As two atoms are brought closer together the energy levels are separated into bands[8]. The width of this band is proportional to the strength of the overlap interaction between the two atoms, i.e. the overlap of their atomic wavefunctions.[8]

The Hamiltonian of a crystal lattice can be written as

$$H = H_{at} + \Delta U(\mathbf{r}), \tag{5}$$

where $\Delta U(\mathbf{r})$ contains the corrections to the atomic potential required to produce the periodic potential of the crystal [11]. More precisely we could form a lattice of ions with lattice vectors $\mathbf{R}$, in which case

$$H = \frac{-\hbar^2}{2m}\nabla^2 + \sum_{\mathbf{R}} U^{at}(\mathbf{x} - \mathbf{R}), \tag{6}$$

where $U^{at}(\mathbf{x})$ is the potential of the atom at our lattice site and is periodic by construction. This is still a single particle Hamiltonian, the difference is that one electron now feels the potential of all the atoms in the lattice.

Wave functions that could satisfy this Hamiltonian can be found by making the ansatz

$$\phi_{\mathbf{k},n}(\mathbf{x}) = \frac{1}{\sqrt{N}} \sum_{\mathbf{R}} e^{i\mathbf{k}\cdot\mathbf{R}} a_n^{at}(\mathbf{x} - \mathbf{R}), \tag{7}$$

where we pick $a_n^{at}(\mathbf{x})$ to be the atomic orbitals. Note that this wavefunction satisfies the Bloch theorem, $\phi_{\mathbf{k},n}(\mathbf{x} + \mathbf{R}) = e^{i\mathbf{k}\cdot\mathbf{R}}\phi_{\mathbf{k},n}(\mathbf{x})$, but that it is not an eigenstate of the Hamiltonian. The full solution to the crystal Schrödinger equation is given by a linear combination of these wave functions

$$\psi_{\mathbf{k},n}(\mathbf{x}) = \sum_m C_{n,m}\phi_{\mathbf{k},m}(\mathbf{x}). \tag{8}$$

To find the ground state we must minimize the energy under the constraint that this wave function stays normalized. This can be done by minimizing

$$\langle\psi_{\mathbf{k},n}|H - E|\psi_{\mathbf{k},n}\rangle = \sum_{m,m'} C_{nm}^* C_{nm'}\langle\phi_{\mathbf{k},m}|H - E|\phi_{\mathbf{k},m'}\rangle. \tag{9}$$

Through variation with respect to $C_{n,m}^*$ we find

$$\sum_{m'} C_{nm'}\langle\phi_{\mathbf{k},m}|H - E|\phi_{\mathbf{k},m'}\rangle = 0. \tag{10}$$

This is just a huge linear system consisting of the matrix elements $H_{mm'}(\mathbf{k}) = \langle\phi_{\mathbf{k},m}|H|\phi_{\mathbf{k},m'}\rangle$ and $S_{mm'}(\mathbf{k}) = \langle\phi_{\mathbf{k},m}|\phi_{\mathbf{k},m'}\rangle$, the overlap integrals. Diagonalizing the matrix $\langle\phi_{\mathbf{k},m}|H - E|\phi_{\mathbf{k},m'}\rangle$ should then yield the band structure of the system.

2.6.1 Tight binding on two atoms

As an example we can solve this for two coupled atoms. In matrix form we can write

$$\det\begin{pmatrix} H_{11} - ES_{11} & H_{12} - ES_{12} \\ H_{21} - ES_{21} & H_{22} - ES_{22} \end{pmatrix} = 0. \tag{11}$$

This equation can be simplified a bit further by noting that orbitals localized on the same atom are orthonormal, thus $S_{11} = S_{22} = 1$. Furthermore, due to the hermiticity of the Hamiltonian we have that $H_{12} = H_{21} = t$, the hopping parameter. Assuming the atoms are of the same element we can say that $H_{11} = H_{22} = \epsilon$ which is called the on-site energy. Finally we write the overlap integrals as $S_{12} = S_{21} = s$. Equation 11 then reduces to

$$\det\begin{pmatrix} \epsilon - E & t - Es \\ t - Es & \epsilon - E \end{pmatrix} = 0 \tag{12}$$

which can be solved by hand to find two solutions,

$$E_+ = \frac{\epsilon + t}{1 + s} \tag{13}$$

and

$$E_- = \frac{\epsilon - t}{1 - s}. \tag{14}$$

These solutions correspond to the two orbitals forming a bonding or antibonding orbital together. This is illustrated in figure 3a. The bonding solution corresponds to the two electron wave functions having a positive amplitude on both nuclei. The antibonding solution has one wavefunction with positive amplitude and the other with negative amplitude. Adding these together means that in the bonding solution the electrons are more likely to sit between the nuclei while for the antibonding solution there is a nodal point between the nuclei, meaning they cannot sit there. The bonding solution corresponds to the energy E_+ and the gradient of its wavefunction is smoother than that of the antibonding solution. Because of this the kinetic energy is lowered, making the E_+ solution the lower energy of the system.

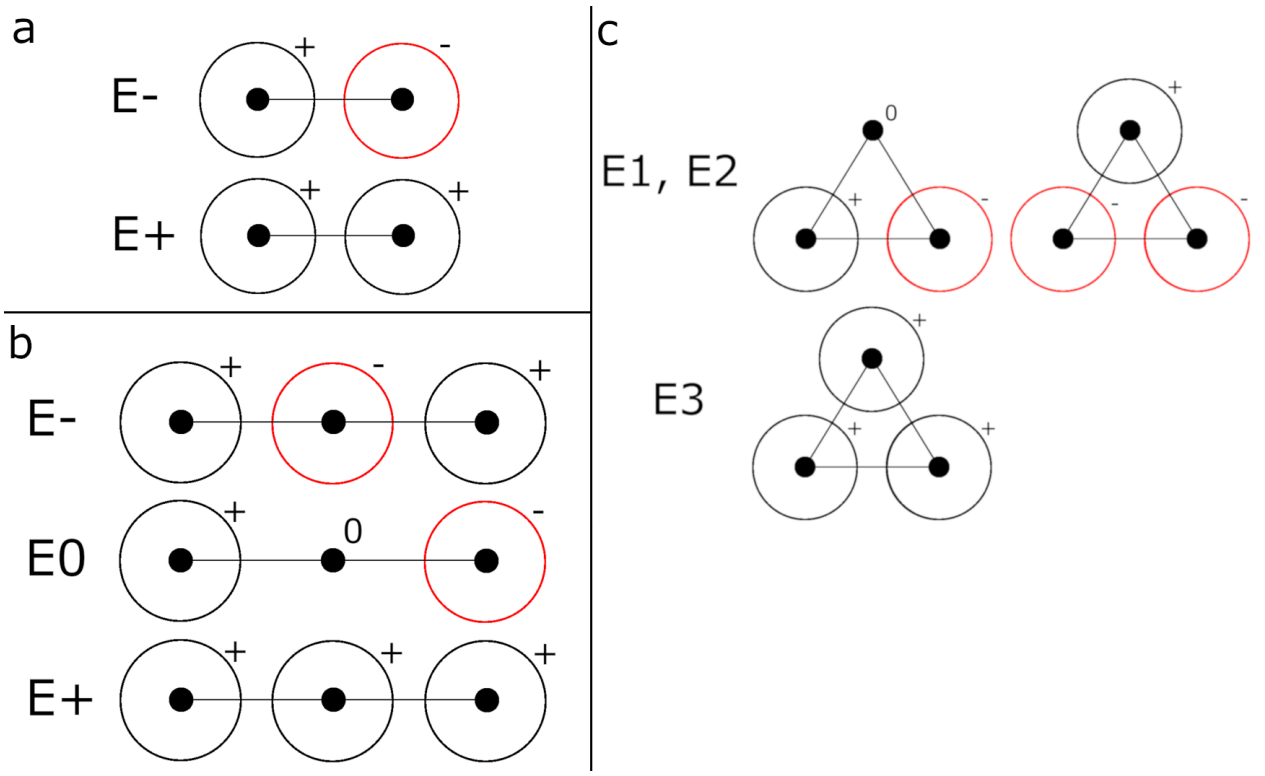

Figure 3: **Schematic illustration of the wavefunction localization in the tight-binding approach. a-c.** Bonding and antibonding states on for resp. the dimer, linear and triangular trimer. The black circle implies a positive amplitude for the wavefunction and the red circle a negative amplitude. Energies corresponding to the states are indicated. Postive amplitudes mix into a bonding orbital while positive and negative mixes into an antibonding orbital.

2.6.2 Tight binding on a linear chain of three atoms

In a similar way we can determine the tight binding equations for a linear chain of three atoms. In that case we get the matrix equation

$$\det \begin{pmatrix} H_{11} - ES_{11} & H_{12} - ES_{12} & H_{13} - ES_{13} \\ H_{21} - ES_{21} & H_{22} - ES_{22} & H_{23} - ES_{23} \\ H_{31} - ES_{31} & H_{32} - ES_{32} & H_{33} - ES_{33} \end{pmatrix} = 0. \tag{15}$$

In addition to the 2 atom case we now also make the simplifications that the overlap between the outer atoms is vanishingly small, so $S_{13} = S_{31} = 0$ and $H_{13} = H_{31} = t'$, the next nearest neighbor hopping parameter. This leads to the system

$$\det \begin{pmatrix} \epsilon - E & t - Es & t' \\ t - Es & \epsilon - E & t - Es \\ t' & t - Es & \epsilon - E \end{pmatrix} = 0 \tag{16}$$

which can be solved to obtain three energy levels,

$$E_0 = \epsilon - t', \tag{17}$$

$$E_+ = \frac{4st - t' - 2\epsilon - \sqrt{8t^2 - 8stt' + t'^2 - 16st\epsilon + 8s^2t'\epsilon + 8s^2\epsilon^2}}{4s^2 - 2}, \tag{18}$$

$$E_- = \frac{4st - t' - 2\epsilon + \sqrt{8t^2 - 8stt' + t'^2 - 16st\epsilon + 8s^2t'\epsilon + 8s^2\epsilon^2}}{4s^2 - 2}. \tag{19}$$

The corresponding orbitals are shown in figure 3b. A bonding state is found corresponding with E_+. Note that the state corresponding with E_0 features a nodal point on the center atom, implying that there are only two energy states there.

2.6.3 Tight binding on three atoms in a triangular arrangement

For three atoms in a triangular arrangement, each atom directly neighbors the two others. This leaves us with a similar determinant as for the linear arrangement, but there are no next nearest neighbors, only nearest neighbors. That is why we can simplify $H_{13} = H_{31} = H_{32} = H_{23} = H_{12} = H_{21} = t$ and we must now say that $S_{13} = S_{31} = s$. All the other simplifications still hold. This leads to the determinant

$$\det \begin{pmatrix} \epsilon - E & t - Es & t - Es \\ t - Es & \epsilon - E & t - Es \\ t - Es & t - Es & \epsilon - E \end{pmatrix} = 0 \tag{20}$$

giving the energy levels

$$E_1, E_2 = \frac{\epsilon - t}{1 - s}, \tag{21}$$

which is two fold degenerate, and

$$E_3 = \frac{\epsilon + 2t}{1 + 2s}. \tag{22}$$

For these solutions the corresponding orbitals are shown in figure 3c. The degenerate state corresponds with an antibonding configuration meaning that it will be the state higher in energy than E_3 which corresponds to the bonding state.

This tight-binding approach can be applied to the artificial atoms. Through dI/dV spectroscopy, using the STM, a plot of the Local Density of States can be obtained from which the energies can be read off. This will give the on-site energy, ϵ, for individual atoms, E_+ and E_- for dimers and E_1, E_2 and E_3 for trimers. The above equations can then be solved to obtain t, s and t'.

3 Experimental method

3.1 The scanning tunneling microscope

This experiment has been attempted on two different scanning probe microscopy setups from Scienta Omicron, the Fermi SPM[14] and the LT STM[15]. Figure 4 shows a picture of the LT setup. In panel a) the chamber that houses the actual microscope is shown. A camera is mounted such that it is possible to view the tip and sample inside the microscope. The electronics are connected on the top, next to the LHe and LN2 inlets. Samples can be inserted into or removed from the microscope while maintaining a vacuum by using the black wobblestick.

Panel b) shows the preparation chamber. This chamber is equipped with a sputter gun and an annealing unit. Through sputtering and annealing, the sample can be cleaned and made atomically flat. The white bottles underneath contain the Argon gas used for sputtering and the CO that is to be deposited on the sample. (N.B. The CO is leaked into the microscope while the sample is in, not in the preparation chamber.) The transfer arm is used to bring the sample from the preparation chamber into the microscope while maintaining the vacuum by sliding a magnet over the outer tube such that the inner arm moves.

In panel c) the turbo (pre-) pump which pumps the LT chamber vacuum is shown. Together with the ion pump (housed under the microscope in panel d) it maintains a vacuum of at least 10^{-10} mbar. Panel e) shows 4 active vibration dampers. These dampers register the vibrations of the building and other vibrations caused by people walking, talking, construction work outside etc. They then produce a counter vibration with such a frequency that destructive interference occurs. Letting the table rest on these active vibration dampers thus reduces many sources of noise.

The general layout of the Fermi SPM is almost the same as that of the LT. Both microscopes are connected to a preparation chamber and in all chambers a vacuum is maintained. The main difference between the two systems is the cryostat. The Fermi SPM uses a flow cryostat meaning that a constant flow of liquid nitrogen or liquid helium has to be maintained to keep the temperature stable at 80-90K or 5-15K respectively. The cryostat of the LT does not need a constant flow of LN2 or LHe and can maintain a temperature down to 4.5K for nearly 60 hours. The main benefit of the LT over the Fermi is that samples do not warm up overnight which would cause CO molecules to diffuse off the surface.

Another difference between the two microscopes is the coarse motor. In the Fermi setup the coarse motor moves the sample in a ϕ and r direction while the tip remains in position.

The LT has an x, y, z coarse motor that moves the tip while the sample remains in position. In both setups the fine piezo is connected to the tip.

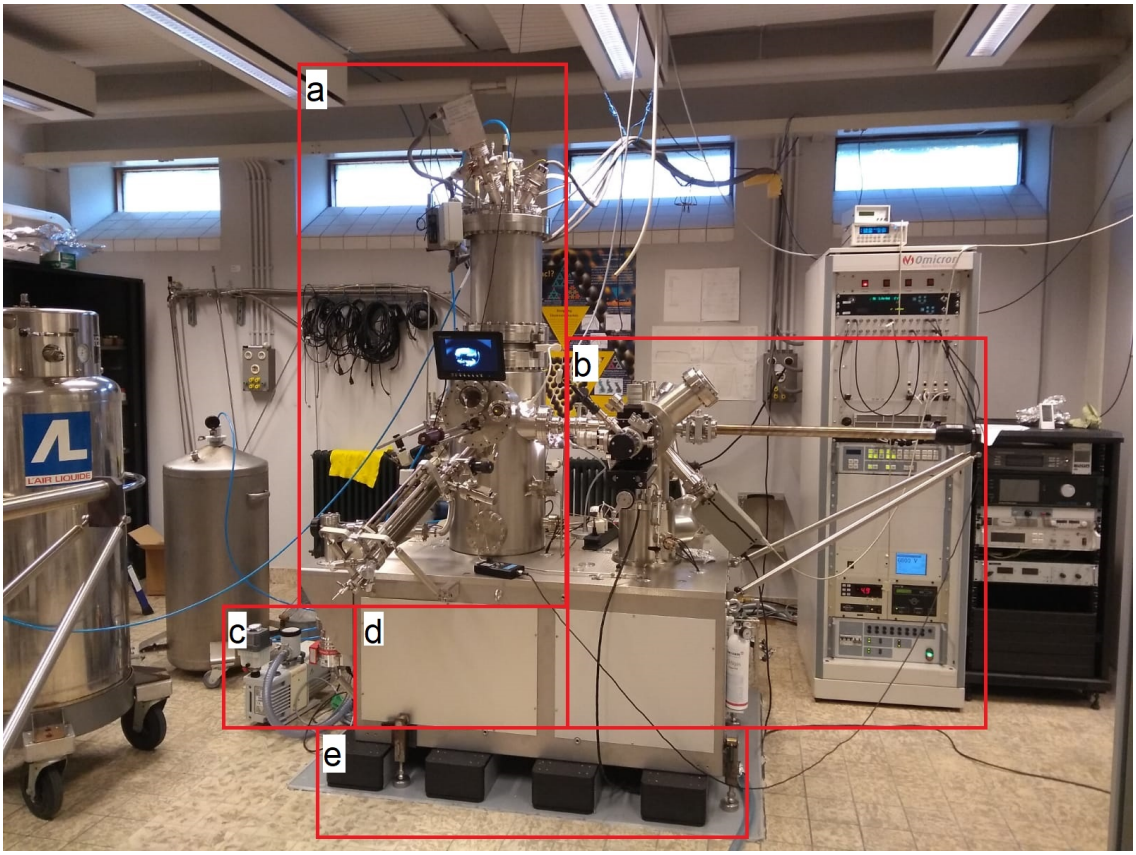

Figure 4: Picture of the LT setup. Panel a shows the LT chamber. Panel b the preparation chamber, c the pump of the LT chamber, d the table housing the TSP and e the active damping system.

3.2 Sample preparation

Because the goal of this experiment is building structures on an atomic scale we require that the copper sample sample used for building is atomically flat (apart for some step edges) and does not have any molecules besides CO adsorbed on its surface. That is why it's important to clean the sample before putting it in the STM and leaking in CO. The surface of the Cu(111) sample is cleaned through several cycles of sputtering and annealing.

Sputtering is the process of bombarding the sample with particles that have a kinetic energy sufficiently high to eject particles off of the solid surface. In this case ionized argon atoms are used. Argon is a noble gas meaning that, besides knocking off some atoms due to the high momentum exchange, the argon won't react with the Cu(111).

The whole process of sputtering and annealing takes place in the sample preparation chamber shown in figure 5. Samples can be put into the preparation chamber by using a load lock shown in panel 5 e). For a proper cycle a base pressure of about 10^{-9} mbar is required in the preparation chamber. As we want to be filling the chamber with argon ions it is important

to switch off the ion pump such as to not overload it. The vacuum can be maintained with a turbo pump as shown in figure 5 f) that should be running for at least three hours before starting the sample preparation. The sputter cannon shown in panel 5c) is connected to a bottle of argon gas (panel 5d)) via some lines. These lines need to be flushed with the argon before the process can start. Once the lines are flushed they can be filled to 1 bar overpressure and a leak valve connecting the argon filled lines to the preparation chamber can be opened. The valve should be opened carefully until the pressure in the chamber reaches 3.5×10^{-6} mbar. At such high pressures electronic connections could cause sparks to fly between the present molecules. To prevent this from happening the pressure gauge should be switched to a range of 0.1 mA, its lowest setting, while sputtering. Sputtering is usually done for 20 minutes each cycle.

After the sputter phase comes the annealing phase. This is done in the heater arm shown in panel 5b) that contains the sample and is connected to the heating unit. The annealing is done through resistive heating at 450°C. Annealing is the process of heating the sample to make the atoms more mobile such that the atoms migrate over the lattice and the amount of defects decreases. However, defects from inside the bulk might migrate towards the surface which is why the annealing phase is only done for 5 minutes.

The procedure described here however is more a guideline than a hard set of rules. Occasionally it can be deviated from based on user experience. When the sample has been through enough cycles of sputtering and annealing it can be moved into the microscope chamber.

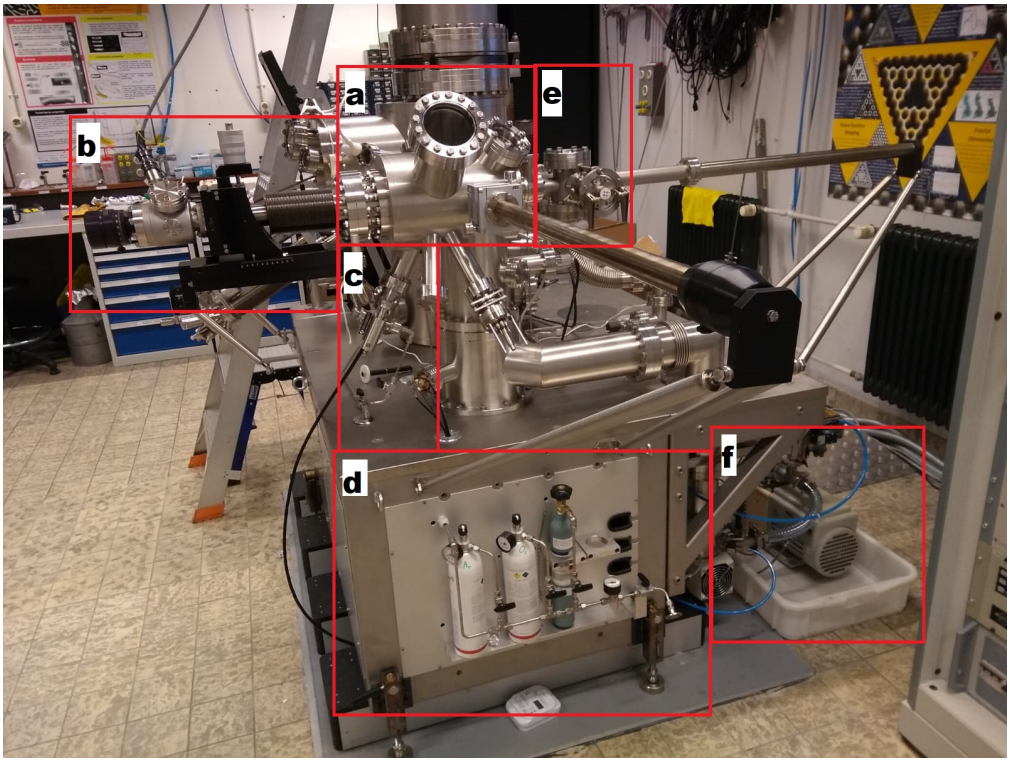

Figure 5: Picture of the LT preparation chamber. Panel a shows the actual chamber. Panel b shows the heater arm, c shows the sputter gun and d shows the argon and CO bottles. Panel e shows the load lock and f shows the turbo pump.

3.3 The LT STM

Figure 6 shows a picture of the LT stage. The stage is thermally coupled to the cryostat above it by copper braids. The LT utilizes an inner cryostat for the liquid helium and an outer cryostat for the liquid nitrogen. By surrounding the LHe cryostat with LN2 the evaporation rate of the LHe is lowered, allowing the sample to stay cool for a longer time. This stage can be suspended on springs to minimize the noise. The sample can slide upside down into a slot as indicated and the coarse motor can move the tip in the x, y, and z directions.

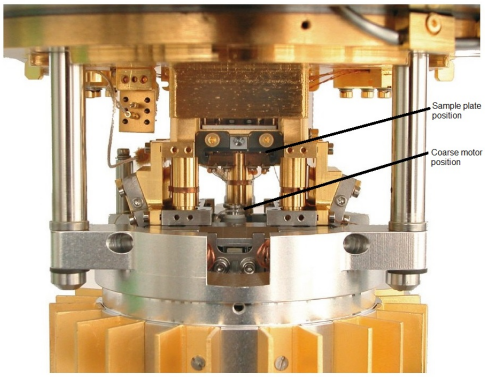

Figure 6: Picture of the LT STM head without its protective shielding. The place where the coarse motor with the tip on it should be is indicated as well as the slot where the sample plate slides into. Picture adapted from Scienta Omicron *LT STM*[15]

The LT STM head is thermally shielded from the outside by two gold-plated rotating shields. Figure 7 shows three wobble stick selectable configurations for the shields. Figure 7a) shows the access for the wobble stick. This way samples can be loaded and unloaded. Panel b) shows the evaporation beam used to evaporate CO onto the Cu(111) surface. When no physical access is needed to the sample, the shields are rotated such that there is only an optical access window minimizing the heat impact as is shown in 7c.

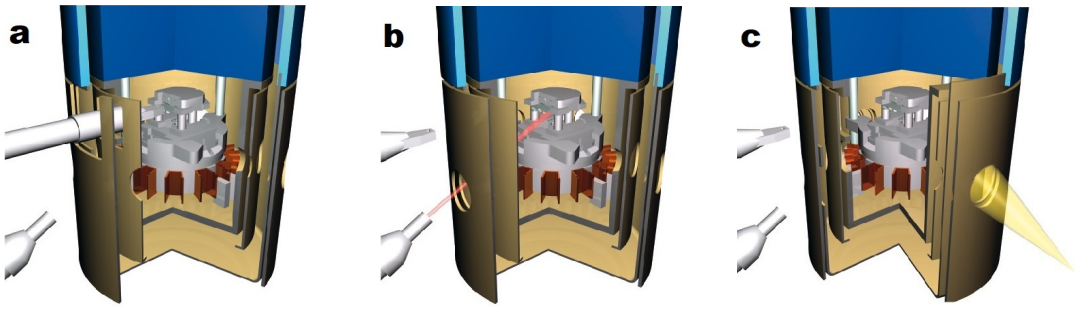

Figure 7: (a) Access for the wobble stick to load and unload tips and samples. (b) Evaporation access to evaporate molecules directly onto the sample. (c) Optical access to view the sample when the shields are closed. Models were taken from Scienta Omicron: *LT STM* `https://www.scientaomicron.com/en/products/low-temperature-spm/further-details#page96`[15]

3.4 The lock-in amplifier

When taking a $\frac{dI}{dV}$ spectrum it is important to know which current signal is coming from the electrons at the energy that the tip is tunneling at and which signal is coming from background noise. To distinguish the actual spectrum from the background noise a lock-in amplifier can be used that does so through phase-sensitive detection. The input signal is

multiplied with a reference signal and this is passed through a low pass filter. This removes any AC signals and only passes a DC signal through where $\omega_{input} = \omega_{ref}$.[16] This way the lock-in amplifier can filter out the desired current signal from the background noise.

The output signal of the lock-in amplifier is given by

$$U_{out}(t) = \frac{1}{T}\int_{t-T}^{t} sin(2\pi\omega_{ref} * s + \phi)U_{in}(s)ds, \tag{23}$$

where U_{in} is the input signal, ϕ the phase and T the integration time. ϕ, ω_{ref} and T can be set on the lock-in amplifier. T should be much larger than the signal period to suppress all unwanted noise and vibrations.

For dI/dV spectroscopy we set $T = 50$ ms, $\phi = 7.26°$ and $\omega_{ref} = 273$ Hz. Furthermore, we can set the amplitude of the reference signal and the sensitivity for which we use $V_{mod} = 10$ mV and 10 mV respectively.

An important step in analyzing these differential conductance spectra is a normalization procedure done by dividing the data by spectra acquired on clean Cu(111). This procedure removes contributions from the slope of the Cu(111) surface state and cancels tip-dependent tunneling matrix elements[4].

3.5 Tip preparation

In the ideal case STM measurements are done with an atomically sharp tip. Getting a tip that is atomically sharp however can prove to be quite a challenge. The tips used are made out of Tungsten wire. To achieve a sharp tip, a z-ramp of a few nanometers into the surface can be done in the hope that pulling the tip out of the surface leaves a lump of atoms dangling from the top that is atomically sharp. The height and speed of this z-ramp can be varied, depending on the current state of the tip. Note that the outer atoms of the tip are the same as the sample surface, Cu(111) in this case.

Another method of tip preparation is the voltage pulse. By applying a voltage pulse between 1V and 10V to the tip some of the outer atoms can be ejected from it and hopefully leave a sharper tip. This method is especially useful when the tip has picked up an unwanted molecule, i.e. a CO while scanning.

Tip preparation remains a process of trial and error. For this experiment a good way of determining the sharpness of the tip is to look at the depth that CO molecules are imaged as. Since CO molecules show op as a dip in STM images, in feedback mode the tip has to go down by a few nanometers to maintain the same current setpoint. If the tip has to go down by roughly 0.03 nm that is a good indication that the tip is more or less atomically sharp or at least not not very blunt.

4 Results and discussions

4.1 The work function above CO

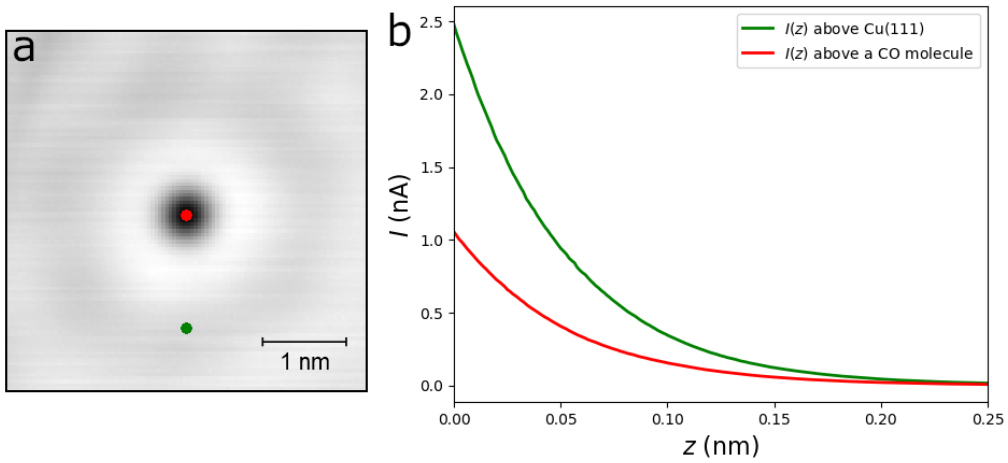

Figure 8: **a.** Scan of a single CO molecule taken at a bias 0.100 V and a current setpoint of 500 pA. **b.** $I(z)$ spectroscopy recorded on Cu(111) (green) and above a CO molecule (red) at the sites indicated in a.

The work function above carbon monoxide was determined by recording an $I(z)$ profile at different points along a line going over the CO molecule. This process is illustrated in figure 8. Panel a) shows a CO molecule and the $I(z)$ spectra shown in panel b) were taken at the sites of the corresponding color. Since $I(z)$ satisfies the exponential proportionality 1 we can take the logarithm of these curves and determine the work function ϕ for each point. This then yields a work function profile that compares the work function above CO against that above clean Cu(111). This was done along a line of 100 points for a single CO and along a line of 150 points for two CO molecules. The two molecules were moved closer together in increments of a from a distance of $7a$ to a, where $a = 0.255$ nm, the nearest neighbor distance of Cu(111).

The obtained work function profiles are shown in figure 9a-h. For each profile the average Cu(111) work function was determined by cropping the data to only the parts left and right of the CO dips and averaging. By manually fitting Gaussian expressions of the form $y = a * \mathrm{Exp}(-(x-b)^2/c) + d$ and reading the parameter a of the best fitting model, the work function above the CO molecules was determined. These numerical results are shown in table 1.

To quantify the uncertainty in the numerical results the standard deviation of $\phi_{Cu(111)}$ was determined for each profile. Averaging over all profiles yields a mean standard deviation of $\sigma_{\phi_{Cu(111)}} = 0.03$ and because these values were used as a baseline the uncertainties in ϕ_{CO} and $\phi_{CO} - \phi_{Cu(111)}$ were also set to 0.03. Only when the CO molecules were at a distance $R = 2a$ the sum of two Gaussians had to be fitted under the constraint that the peak positions were roughly 0.5 nm apart. This resulted in a rough estimate for the best fit, shown in 9g, which is why we set the uncertainty in those values to be 0.08.

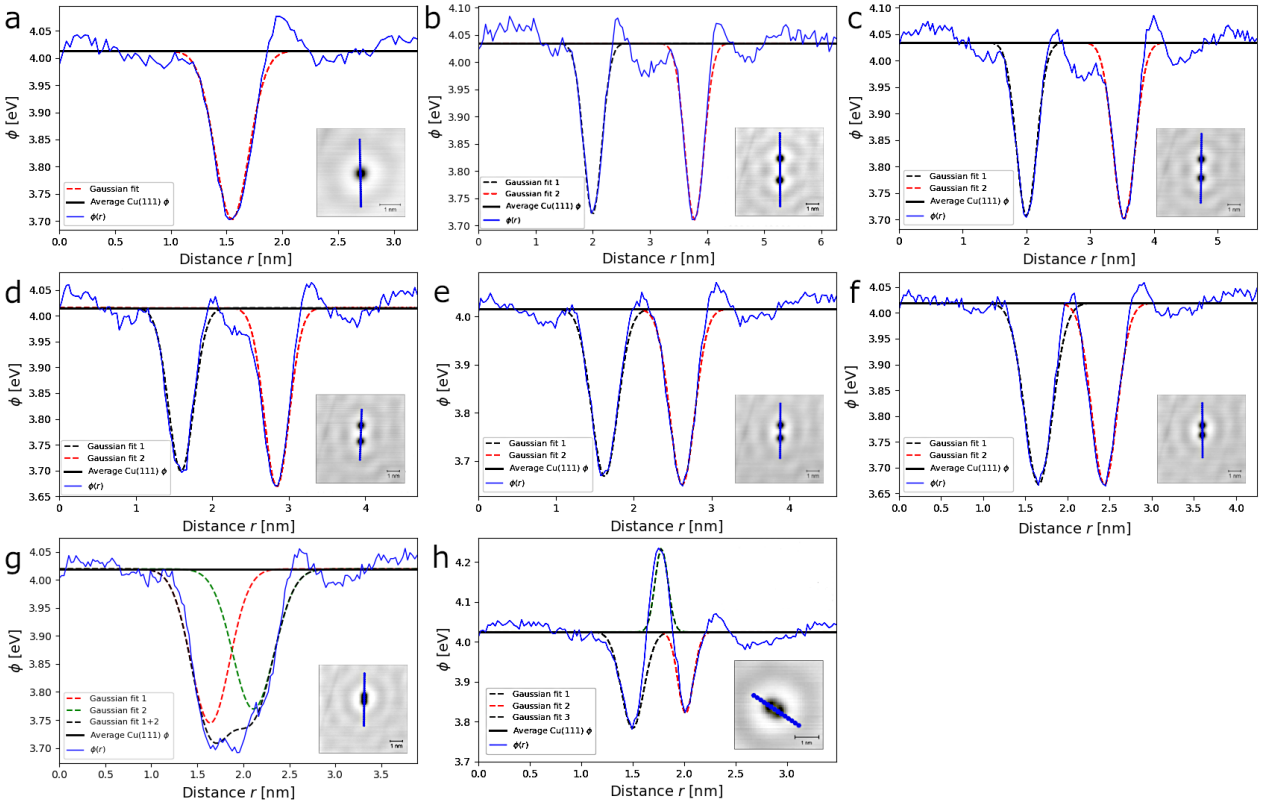

Figure 9: **Work function profiles over a CO molecule along the inset line. a**, Work function profile over a single CO molecule. **b-h**, Work function profile over two CO molecules separated by a distance $7a$, $6a$, $5a$, $4a$, $3a$, $2a$, and a respectively. In each image the black line shows the average Cu(111) work function and the Gaussian fits were used to determine the value of ϕ_{CO}. Inset images: Scan at bias 0.100 V and current setpoint 500 pA with the line spectroscopy profile drawn. Scale bar: 1nm.

Table 1: Quantitative work function values above the clean Cu(111) surface and CO molecule(s) adsorbed on the surface.

Distance & Figure	$\phi_{Cu(111)}$ ($\pm$0.03) (eV)	ϕ_{CO} ($\pm$0.03) (eV)	$\phi_{CO} - \phi_{Cu(111)}$ ($\pm$0.03) (eV)
Single CO (Fig 9a)	4.01	3.70	-0.31
$R = 7a$ (Fig 9b)	4.03	3.72	-0.31
$R = 6a$ (Fig 9c)	4.03	3.70	-0.33
$R = 5a$ (Fig 9d)	4.02	Left: 3.70, Right: 3.67	-0.32 & -0.35
$R = 4a$ (Fig 9e)	4.02	Left: 3.67, Right: 3.65	-0.35 & -0.37
$R = 3a$ (Fig 9f)	4.02	3.67	-0.35
$R = 2a$ (Fig 9g)	4.02	Left: 3.74, Right: 3.77 ($\pm$0.08)	-0.28& -0.25 ($\pm$0.08)
$R = a$ (Fig 9h)	4.03	Left: 3.79, Middle: 4.24, Right: 3.83	-0.24, 0.21 & -0.20

Since the work function value on Cu(111) should be constant we can average the values in column two to find

$$\phi_{Cu(111)} = 4.02 \pm 0.03 \text{ eV}.$$

This value is lower than the value of 4.98 eV found in literature [8] but this difference is likely caused by the experimental dependency on the state of the tip. The work function above a single CO molecule is found to be

$$\phi_{CO} = 3.70 \pm 0.03 \text{ eV}$$

and for two CO molecules being moved closer together this value does not seem to change significantly. The main exceptions are the cases where $R = 2a$ and $R = a$, where the work function above the CO molecules seems to decrease less than in other configurations, even increasing above the Cu(111) level in center of the $R = a$ configuration.

Several interesting features can be noted about the plots from figure 9. First of all the work function above a CO molecule is lower than the work function above Cu(111). This result is quite unexpected as it is known that at a bias of 0.100V the tip has to get closer to the surface above a CO to maintain its current setpoint. Since $I(z) \propto e^{-2kz}$ it is only logical that k has to go up when z goes down and I remains constant. The only variable in $k = \sqrt{2m\phi}/\hbar$ however, is the work function, ϕ, implying that ϕ gets larger above a CO molecule compared to above the bare Cu(111) surface. The experiment shows the opposite.

These results are corroborated by a density functional theory (DFT) calculation shown in figure 10. There a tip was modeled to travel along a line over the surface and over two adsorbed CO molecules as shown in 10 a, simulating the experiment done. From this the recorded electrostatic potential was extracted and is shown in 10 b. Apart from some shift w.r.t. the Fermi level of Cu(111) the electrostatic potential is the same as the STM work function. This calculated profile is the same as the experimental profile showing a dip of about 0.3 eV above a CO compared to bare Cu(111). This gives a strong indication that the experimental results are correct and that the theoretical approach of equation 1 breaks down above a CO molecule.

Usually adsorbed molecules and adatoms are imaged as a protrusion rather than a dip in the STM. Interestingly CO gets imaged as a protrusion whenever the tip is terminated with a CO molecule. Alexander Gustafsson and Magnus Paulsson investigated this effect through density functional theory (DFT) calculations. [13] Their calculations suggest that the dip in tunneling current above a CO is due to an interference effect between the tip and substrate wavefunctions. Furthermore, they show that the basic assumption of the Bardeen approximation on which the proportionality 1 relies breaks down above a CO, this assumption being that the potential of the tip does not disturb the substrate wavefunctions. This is a strong indication that other terms in the tunnel current play a role that results in the tunnel current as well as the work function being lowered at the same time.

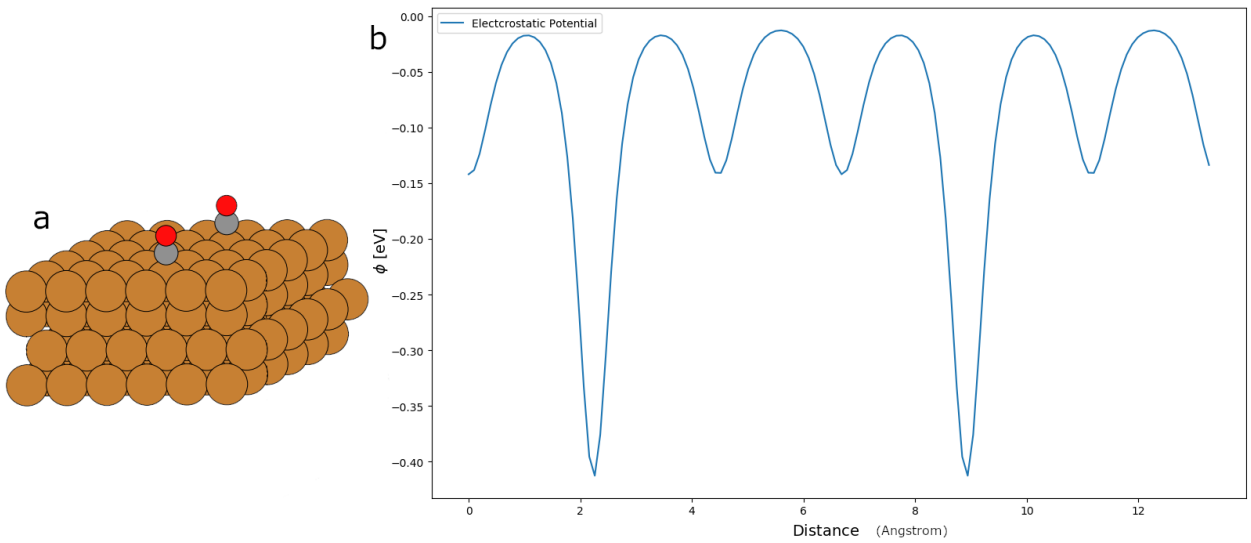

Figure 10: **Density functional theory calculation of CO on Cu(111). a.** Configuration of the CO molecules on the Cu(111) surface used in the calculation. **b.** Calculated profile of the electrostatic potential.

4.2 Artificial atoms

A Cu(111) sample was prepared according to the preparation steps shown in table 6 in appendix A and moved into the LT STM. CO was leaked in at 1.3×10^{-8} mbar for 60 seconds and artificial atoms of varying size have been built. For scanning the bias voltage was set at 0.100 V and a feedback loop with a current setpoint of 30 pA was maintained. CO manipulation was done at a bias voltage of 0.02 V and a current setpoint of 25 nA.

To create the artificial atoms the CO molecules were arranged in a hexagonal pattern with edges of $2a$, $3a$, $4a$ and $5a$, where $a = 0.255$ nm, the Cu(111) lattice constant. Several of these artificial atoms can be seen in figure 11. On the atoms with edges of length $4a$ and $5a$ additional CO molecules were added to function as blockers that decouple the atoms from the outside surface state, i.e. confining the electrons to a stronger box.

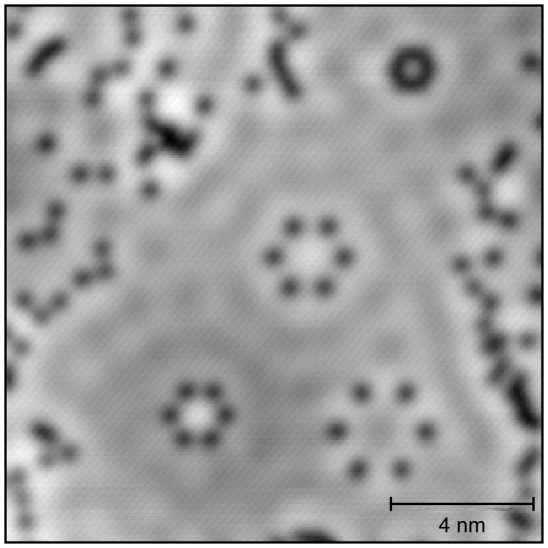

Figure 11: Scan at bias 0.100 V and I-setpoint 30 pA of artificial atoms width edge length $2a, 3a, 4a$ and $5a$ where $a = 0.255$ nm.

Furthermore, hexagonal dimers were created of the atoms with edge length $4a$ and $5a$. On those dimers the blockers were immediately added as results from the individual atoms showed that blockers enhanced the desired effects significantly. No measurements were done on dimers without blockers. For the dimers the

configuration of CO molecules in the middle was altered, effectively weakening or strengthening the bond of the dimers by respectively moving in an extra CO or placing the CO's further apart.

The local density of states of these atoms and dimers was measured by doing dI/dV spectroscopy in the middle of the atoms. Spectroscopy was done at a bias voltage varying between -0.600 V and 0.500 V in increments of 0.002 V every 0.15 s, so taking a total of 500 samples. An intermediate feedback loop with a current setpoint of 1.00 nA was maintained between every sample. The lock-in amplifier was set to an oscillation amplitude of 10 mV and an integration time of 50 ms.

Quantitative values were found by manually fitting Gaussians of the form $y = a * \mathrm{Exp}(-(x-b)^2/c) + d$ to the relevant dI/dV peaks. The parameters a, b, c,and d could then be read off. In all measurements the energy, parameter b, was the desired quantity. In this section I will only present the relevant comparisons between configurations. A database of all the individual spectra and fits is found in table 7 in appendix B.

4.2.1 Comparing atoms of different size

In figure 12 the normalized differential conductance spectra acquired above the centers of the individual atoms of edge length 2-6a are shown. The atoms of edge $2a$ and $3a$ were not blocked with additional CO. Of the atoms of edge $4a$ and $5a$ both an unblocked and blocked version was built and measured. Of the $6a$ atom only a blocked version was made.

Because Cu(111) has a surface state onset at $V = -0.45$[6] the data is cropped to a bias window of -0.4 V to 0.5 V. The peaks in the spectra represent the on-site energy of the s-orbital of the artificial atom. The on-site energies, ϵ, were determined by reading off the center position of Gaussian fits. The uncertainty in these values was determined from the width of the Gaussians.

Note that the on-site energy of the $2a$ atom was beyond the measuring range. A general increase of the local density of states can be observed but the actual position of the peak was unreadable. Furthermore, the spectrum of the $3a$ atom showed 3 more or less distinct peaks in a very broad region. An average was taken and the uncertainty was set to 0.105 to include the whole region.

The general trend in the figure is that the on-site energy is lowered as the size of the atom grows. The atom surface area was calculated by calculating the surface area of a hexagon of edge size $n * a$ ($n = 2, 3, 4, 5, 6$, $a = 0.255$ nm) and subtracting the area that the CO molecules protrude into the hexagon. In the STM CO molecules are imaged with a radius $r_{CO} \approx 0.3$ nm. The surface areas of the atoms and their measured on-site energies are shown in table 2.

The ground state energies of a particle in a two dimensional square and circular box are respectively given by

$$E_0 = \frac{\hbar^2 \pi^2}{2mL^2} \tag{24}$$

and

$$E_0 = \frac{\hbar^2}{2m}\left(\frac{2.4048}{R}\right)^2 \tag{25}$$

where L is the side of the square box and R the radius of the circular box[17]. Both cases

follow a general trend $E \propto \frac{1}{A}$, where A is the area. As a hexagonal shape lies somewhat between the square and circular shape we expect the relation between the on-site energy and the reciprocal surface area to be linear. A plot of the data points from table 2 is shown in figure 13 with a linear relation fitted to the data. The atom with edge type $3a$ was left out because of its huge uncertainty.

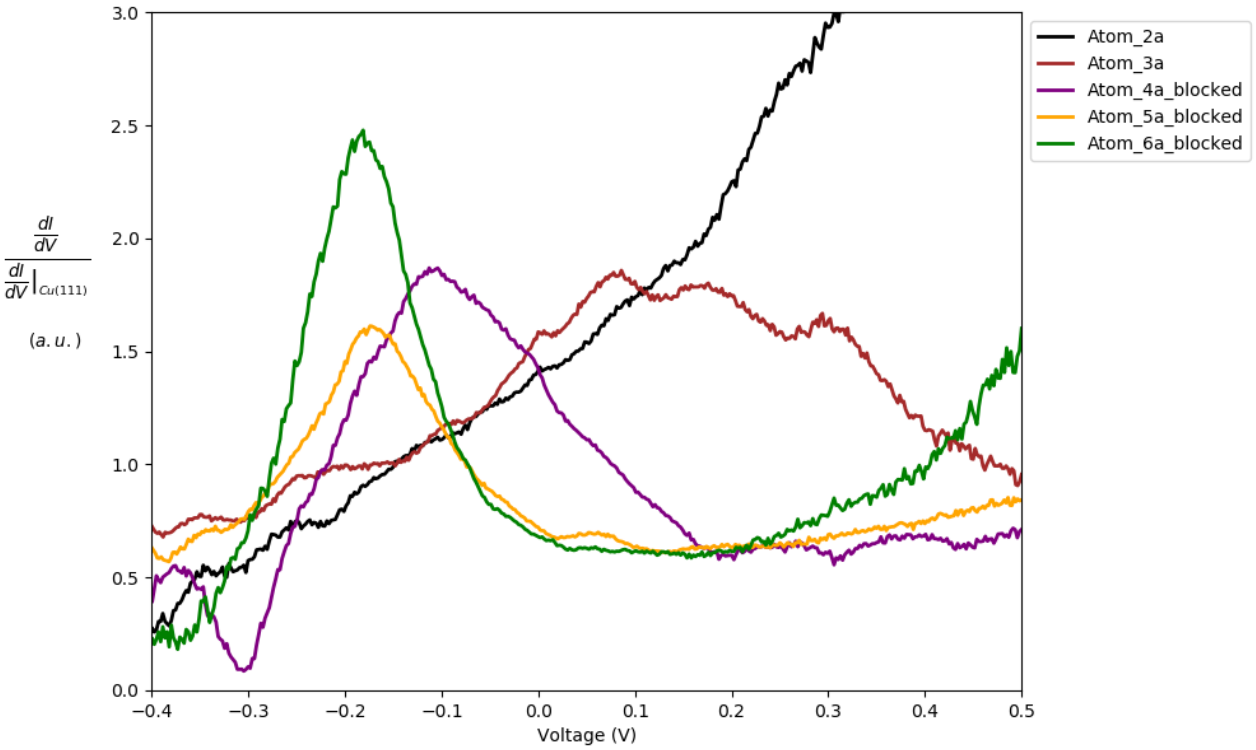

Figure 12: Normalized differential conductance spectra aquired above the centers of hexagonal artificial atoms with edge sizes ranging from $2a$ to $6a$. Sizes $4a$, $5a$ and $6a$ were blocked with additional CO molecules. Individual spectra, designs and scans are shown in appendix B, table 7.

Table 2: Surface area and measured on-site energy of s-type orbitals on the artificial atoms.

Edge type	Surface area (nm^2)	On-site energy ϵ (eV)
$2a$	0.11	n/a
$3a$	0.95	0.18 $\pm$ 0.105
$4a$	2.14	-0.06 $\pm$ 0.03
$4a$ blocked	2.92	-0.11 $\pm$ 0.03
$5a$	3.66	-0.20 $\pm$ 0.02
$5a$ blocked	3.58	-0.17 $\pm$ 0.02
$6a$ blocked	3.82	-0.19 $\pm$ 0.015

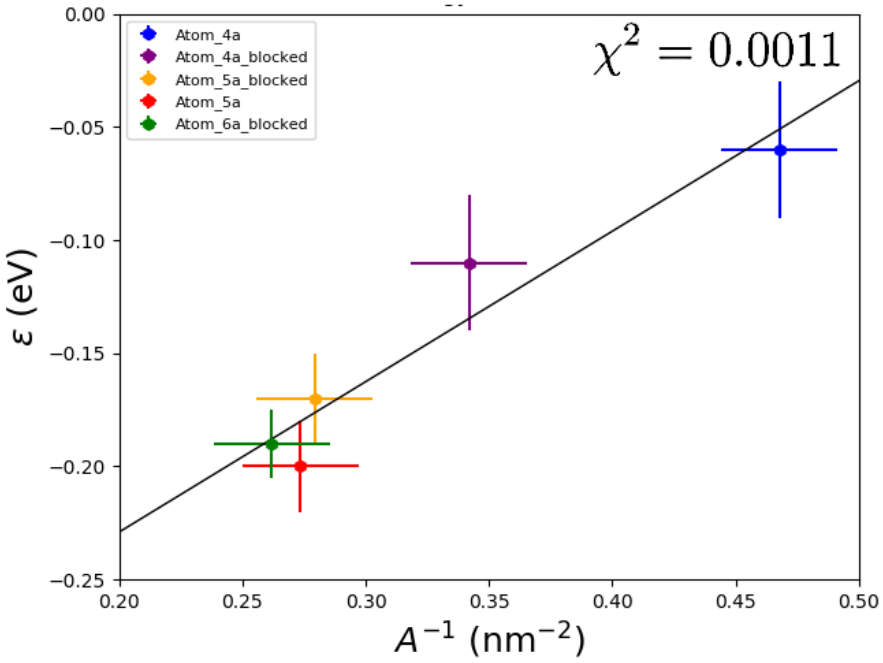

Figure 13: The measured on-site energy ϵ set out against the reciprocal of their atoms surface area A. A linear model of the form $y = a*x+b$ is fitted with fitting parameters $a = 0.66\pm0.20$ eVnm^2, $b = -0.36 \pm 0.065$ eV. $\chi^2 = 0.0011$.

4.2.2 The effect of blockers

In section 4.2.1 we already saw that of the $4a$ and $5a$ edge atom both an unblocked and a blocked version were built. In figure 14 we investigate the difference these blockers make by comparing the spectra of the unblocked and the blocked version.

First of all it can be noted the the density of states increases when an artificial atom is blocked. The peak in the dI/dV spectrum becomes sharper and higher in both cases. The interpretation is that fewer states can protrude into the outside, effectively decoupling the atom more from the environment and enhancing its atomic behavior.

Another difference is the position of the peak. In section 4.2.1 the on-site energy was different for the unblocked and blocked versions. This difference can be attributed to the change in the atoms surface area when blockers are added. Particularly on the $5a$ atom the presence of extra CO molecules removes a part of the atoms surface area, effectively making it smaller thus elevating the on-site energy.

On the $4a$ atom the blockers were positioned a bit outside of the hexagon. On average this lead to a larger surface area with less coupling to the environment. This larger surface area leads a lowering of the on-site energy. This difference could already be seen in figure 13. The position of the blockers was chosen like this because it is more likely to block artificial lattices in a similar configuration.

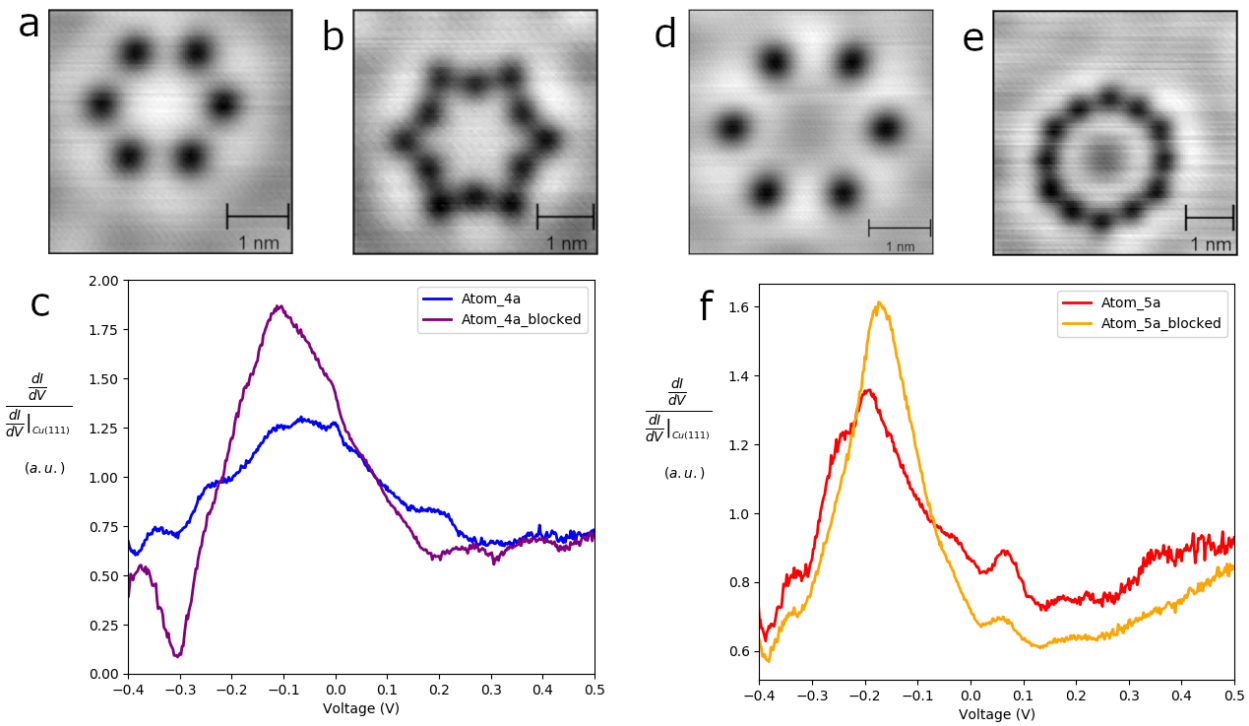

Figure 14: **Comparison between unblocked and blocked versions of the** $4a$ **and** $5a$ **edge type artificial atoms. a, b, d, e.** Scans at bias 0.100 V and I-setpoint 30 pA of resp. the $4a$ and $5a$ edge atoms. **c, f.** Normalized differential conductance spectra comparing the unblocked and blocked version of the $4a$ and $5a$ edge atoms.

4.2.3 P-like orbitals in artificial atoms

In section 4.2.1 the measured on-site energies of the artificial atoms were discussed. These energies were measured in the centers of each atom where the s orbital is most dominant. In the $5a$ and $6a$ atoms however, a relatively high intensity is found at the edges of the atom when scanning at a bias of 0.100 V. This intensity indicated the presence of the p orbitals in that energy range. To characterize these p-like orbitals differential conductance spectra were taken above the edges of $5a$ blocked and $6a$ blocked atoms. These spectra are shown together with the spectra above the center in figure 15.

The on-site energies of the s orbital are still visible in the same position as in figure 12 though their intensity has clearly diminished at the edge compared to the center. In addition both edge spectra feature a peak at higher energy, this corresponds to the on-site energy of the p orbital. In the same way as described in section 4.2.1 Gaussian fits were made and the energies were found to be

$$\epsilon_{p_{5a}} = 0.21 \pm 0.022 \text{ eV}$$

and

$$\epsilon_{p_{6a}} = 0.17 \pm 0.020 \text{ eV}$$

for the $5a$ and $6a$ atom respectively.

Similar to the on-site energies of the s orbitals a shift towards lower energy is observed as the atom surface area grows. However, this shift seems to be larger for the p orbitals, having

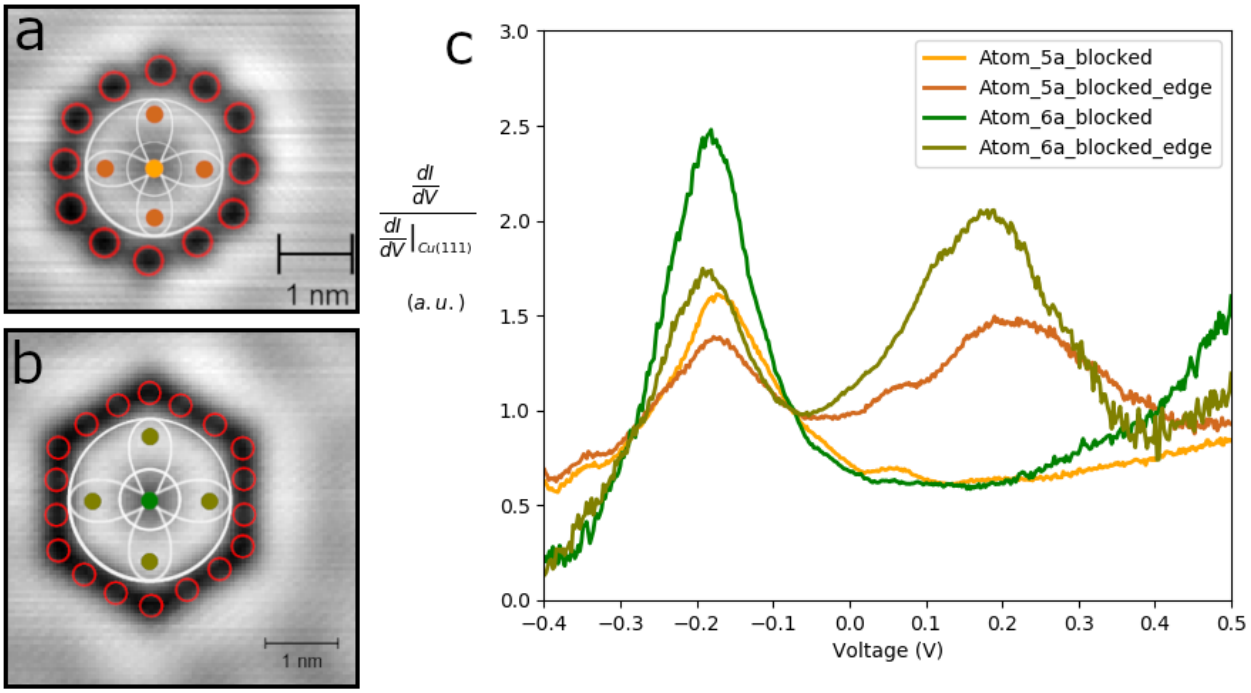

Figure 15: **S and p orbitals on artificial atoms. a. & b.** Scan at 0.100 V and 30 pA of respectively the 5a and 6a atom with blockers. CO positions are indicated in red. In white an impression of s and p orbitals is drawn. **c.** Normalized differential conductance spectra acquired at the positions indicated with the same color in a & b. Individual spectra and Gaussian fits are shown in appendix B, table 7

a difference of 0.04 eV between the 5a and the 6a atom while that difference is only 0.02 eV for the s orbitals. This behavior is to be expected as a 2d particle in a box has an energy

$$E = \frac{\hbar^2 \pi^2}{2mL^2}(n_x^2 + n_y^2), \tag{26}$$

implying that the on-site energy of higher modes (p orbitals) should scale steeper with $1/L^2$ than the s orbital modes.

4.2.4 Creating dimers and the influence of barrier geometry on coupling strength

When placed next to each other, two artificial atoms can couple in a way similar to regular atoms. The only difference is that the strength of the coupling is now tunable by placing more or fewer CO molecules in the middle between the two atom sites. This effect was investigated by building dimers of the blocked 4a and 5a type atoms.

The coupling was strengthened by placing the inner CO molecules further apart, lowering the scattering barrier between the center sites and the coupling was weakened by placing extra CO molecules in between the atom sites, increasing the scattering barrier. In figure 16 the designs (a-c), scans (d-f) and spectra (g-i) of the blocked 5a dimers with a higher, normal and lower scattering barrier are shown. The designs, scans and spectra of the blocked 4a dimers can be found in table 7 in appendixB.

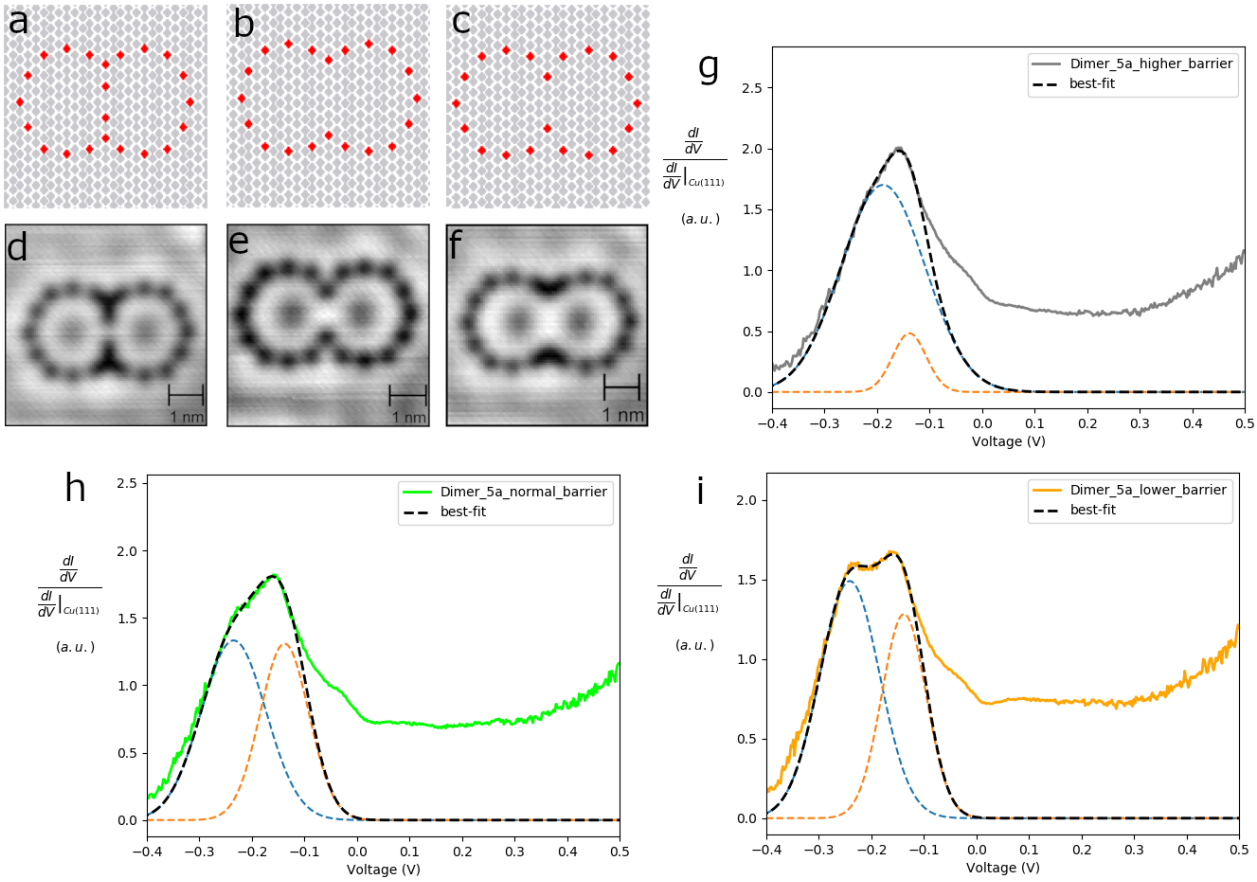

Figure 16: **Different barrier geometries in an artificial dimer of edge length 5a with blockers. a-c.** Position of the CO molecules on the Cu(111) surface. with resp. a higher, normal and lower barrier. **d-e.** Scans at bias 0.100 V and I-setpoint 30 pA corresponding to the designs in resp. a, b and c. **g-i.** Normalized differential conductance spectra acquired in the centers of the dimers atoms. The dashed black line shows the sum of two Gaussians (dashed blue and orange) fitted to only the peaks of interest.

On the s orbital dI/dV peaks we can see that the stronger coupled dimers feature two distinct peaks while a single atom only features one peak. This result agrees with the theory of tight binding, as discussed in section 2.6, where a splitting of energies is calculated when coupling two s orbitals together. We thus expect the peaks in the dimers to consist of the sum of two Gaussians.

Because the scattering of the states is of the same origin, we expect the two Gaussians to have a similar width and amplitude. Under these constraints we fit the sum of two Gaussians to the desired peaks and by reading off the peak position of the original Gaussians we know the value of E_+ and E_- in equations 13 and 14.

Furthermore, we remark that the barrier strength was altered by adding or removing CO molecules to the middle of the dimer. As discussed in section 4.2.2 this will impact the surface area of the artificial atoms thus altering their on-site energy. We calculate the altered surface areas by calculating the surface area of a dimer with a method similar to the one described in section 4.2.1 and dividing the result by two. For the different barrier geometries

we then add or subtract the surface area a CO molecule occupies. Then we can invoke figure 13 from section 4.2.1 to find the new on-site energies.

With the values of E_+, E_- and the new on-site energies we can use equations 13 and 14 to calculate the hopping parameter, t, and the overlap integral, s. These values are shown in table 3. The uncertainties were estimated from the width of the Gaussians and from the uncertainties in the fit of figure 13.

Table 3: Tight binding parameters for dimers of the $4a$ and $5a$ blocked edge type with varying barrier height.

Dimer type	E_+ ± 0.070 (eV)	E_- ± 0.055 (eV)	ϵ ± 0.021 (eV)	t ± 0.073 eV	s ± 0.073
$4a$ high	-0.122	-0.001	-0.102	-0.102	0.669
$4a$ normal	-0.150	-0.021	-0.128	-0.121	0.659
$4a$ low	-0.181	-0.015	-0.160	-0.156	0.747
$5a$ high	-0.189	-0.138	-0.164	-0.029	0.019
$5a$ normal	-0.235	-0.138	-0.187	-0.050	0.010
$5a$ low	-0.241	-0.138	-0.191	-0.057	0.029

Several things can be noted about the values in table 3. First of all we see a trend where the hopping, t becomes smaller as the barrier is increased. The orbital overlap however is larger on the dimers with the higher barrier. Intuitively this is incorrect as there is less space for the orbitals to protrude out of their own atom area. The error here can be attributed to the fact that we tried to fit two Gaussians. In figure 16g we see that the amplitude of the Gaussians is quite different. From this we can argue that the peak exhibits the behavior of only one Gaussian and that the addition of 2 CO molecules heightened the barrier in such a way that it is no longer a dimer but just two individual decoupled atoms lying next to each other. From fitting a single Gaussian manually we find the peak at an energy $E = 0.16$ eV for the $5a$ dimer which lies close to the on-site energy $\epsilon = -0.164$ invoked from its area and figure 13.

These results were corroborated with a theoretical LDOS calculation done by Mickey Bramer at the Institute of Theoretical Physics at Utrecht University[18]. The same configurations as in figure 16 a-c)were modeled and the LDOS was calculated. Figure 17 shows the comparison between the differential conductance spectra obtained using scanning tunneling spectroscopy (a & b) and the calculated local density of states (c & d). All spectra from the $5a$ dimer show a remarkable agreement with theory. The spectra from the $4a$ do not show a splitting as clear as the theoretical model. This could be attributed to the fact that these spectra were taken with a different tip that was not ideal for scanning tunneling spectroscopy, inducing background features that could not be compensated for properly. The energies obtained from the Gaussian fits on the $4a$ dimer however were relatively similar to the energies seen on the theoretical model. For this reason we still reported the measured values in table 3.

Note that the theoretical models show no splitting for the dimers with a high barrier. This gives an even stronger indication that the two Gaussians fitted to those spectra (see figure 16g) are unphysical, which is why we can dismiss the corresponding values obtained for t and s.

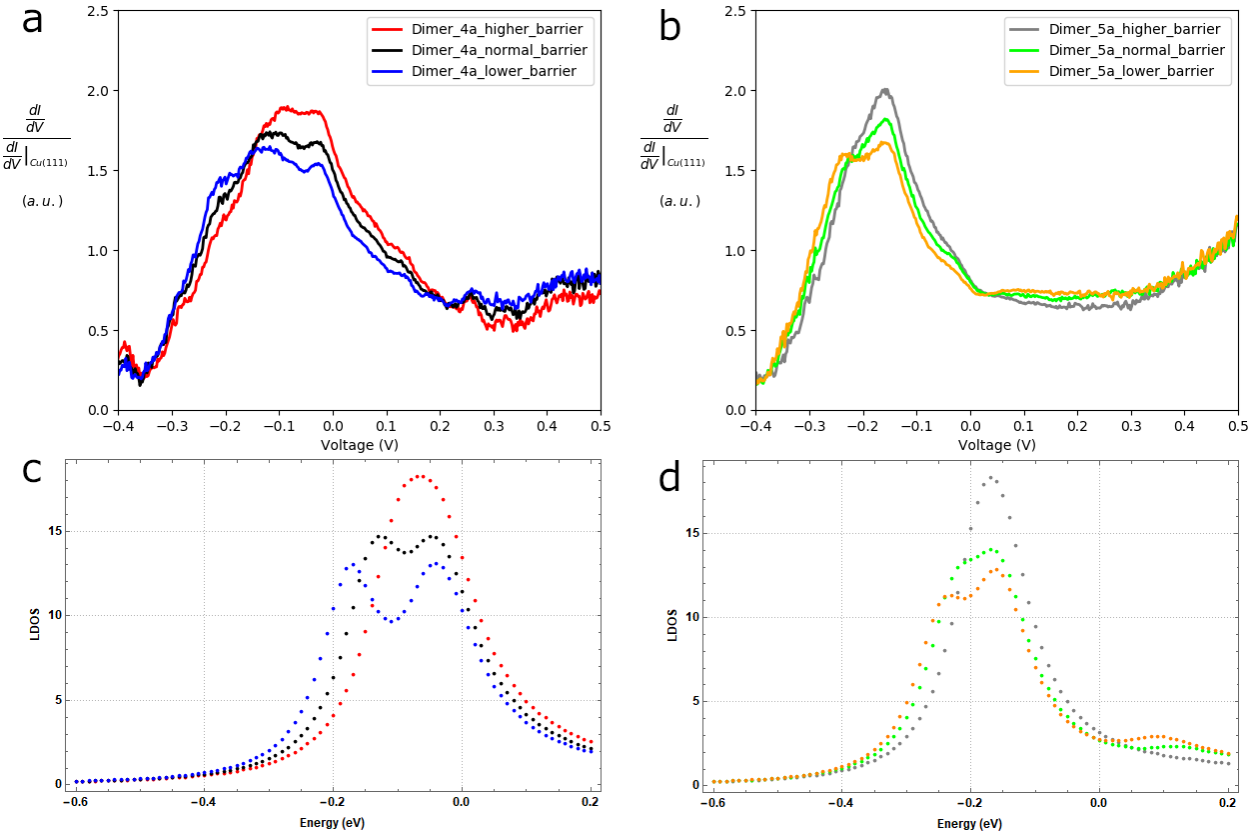

Figure 17: **Comparison between a** $4a$ **and** $5a$ **blocked edge type dimer with different barrier geometries. a,b.** Normalized differential conductance spectra acquired in the centers of the atoms making up the dimers. **c, d** Local density of states of the same structures obtained through muffin-tin simulation[18].

The models for the dimer with a normal and a low barrier show a good agreement with experiment. For the $4a$ dimer the experiment indicates a hopping parameter in the range $t = -0.12$ to $t = -0.16$ eV and orbital overlap in the range $s = 0.66$ to $s = 0.75$. The $5a$ dimer shows a hopping parameter in the range $t = -0.05$ to $t = -0.06$ eV and orbital overlap $s = 0.01$ to $s = 0.03$. The splitting for the configurations with a low barrier is summarized in the molecular orbital diagrams in figure 18. In the MO diagram of the $4a$ dimer we clearly see that the energy of the antibonding state is pushed much higher than that the energy of the bonding state is pushed down. This can be attributed to the high orbital overlap we found.

Most importantly we can conclude from these dimers that both the hopping and the orbital overlap get stronger as the barrier is lowered, as expected from theory. Intuitively, the dimer would turn into one single large atom as the barrier is completely removed but these results do not give a strong indication for this yet.

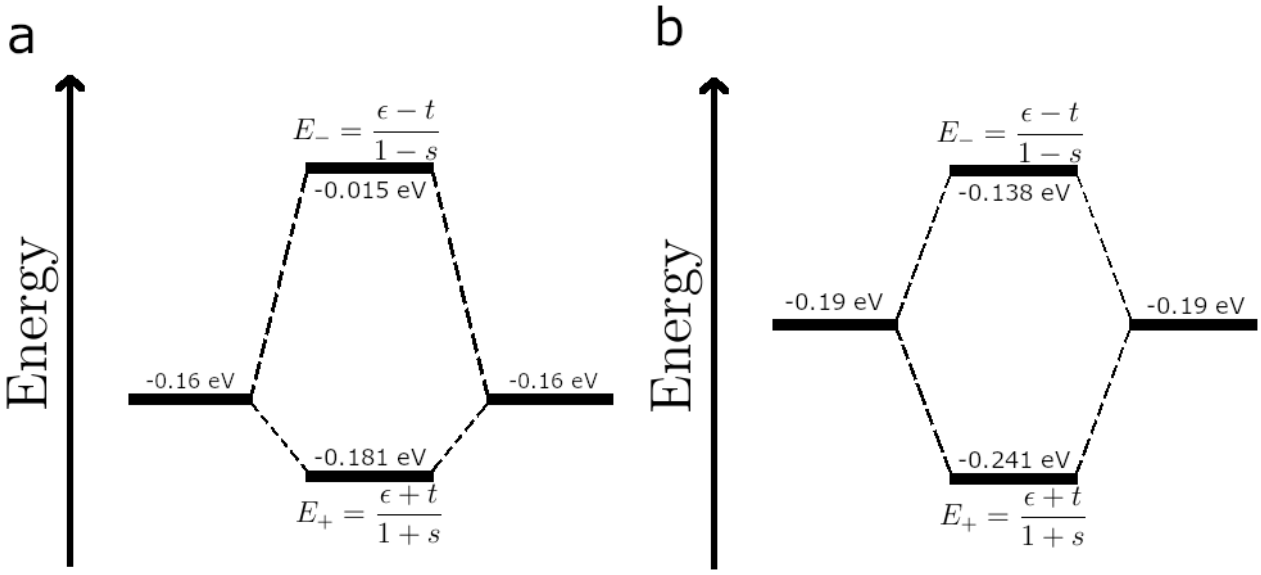

Figure 18: **a.** Molecular orbital diagram of the blocked dimer with edge length $4a$ and a lower barrier. **b.** Molecular orbital diagram of the blocked dimer with edge length $5a$ and a lower barrier. Energetic positions of the orbitals are indicated.

4.2.5 Coupling of s orbitals in a linear and triangular trimer

A linear and a triangular trimer were built out of artificial atoms with a $5a$ blocked edge. The differential conductance was recorded at the sites indicated in figure 19 and the obtained spectra can be seen in table 7 in appendix B. To investigate the coupling of the s orbitals we look at the spectra taken at the centers where they are most prominent. These spectra were taken at the purple and dark green sites for the linear trimer and at the black sites for the triangular trimer. They are shown in figure 20. For the triangular trimer the spectra on the edges (gray) showed peaks for the s orbitals as well, enabling us to get a better estimate for the energies. The energies were obtained by fitting Gaussians. Just as for the dimers we needed to fit the sum of multiple Gaussians to obtain a best fit.

The tight binding solutions for the linear trimer in section 2.6 imply that a splitting into three energy levels should be observed. However, in a linear trimer one of the three states will feature a nodal point in the center atom, meaning that we should observe only two energy levels there. This splitting into two levels is observed in the center atom of figure 20 b. The outer atom spectra in figure 20a however feature only one peak. From theory we know that this peak should consist of three Gaussians and from figure 20b we can determine the parameters of two of those Gaussians. Constraining those two to be the same in the purple spectrum we can obtain a best fit made of three Gaussians, giving us the energy splitting we expected. The obtained energies are shown in table 4. With these energy values and with a new on-site energy invoked from figure 13 we can use equations 17, 18 and 19 to find the hopping parameter, t, the orbital overlap, s and the next nearest neighbor hopping t' in the linear trimer.

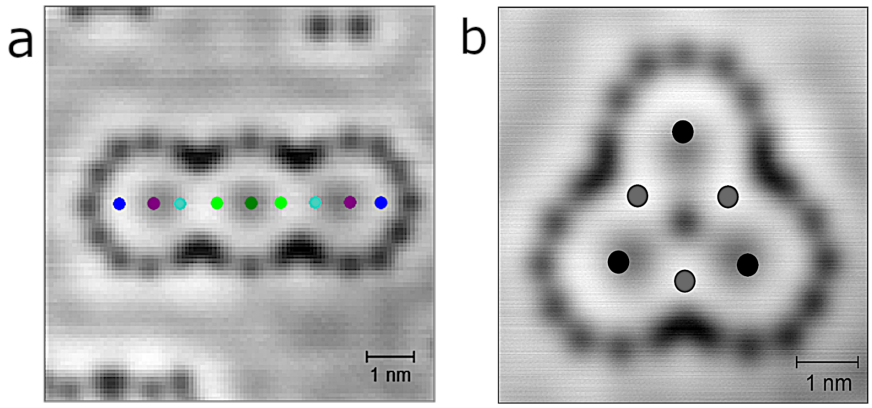

Figure 19: STM scans of the linear and triangular trimer of the 5a blocked edge type. Scans were taken at a bias of 0.100 V and a current setpoint of 30 pA. Colors correspond with different positions where dI/dV spectroscopy was taken.

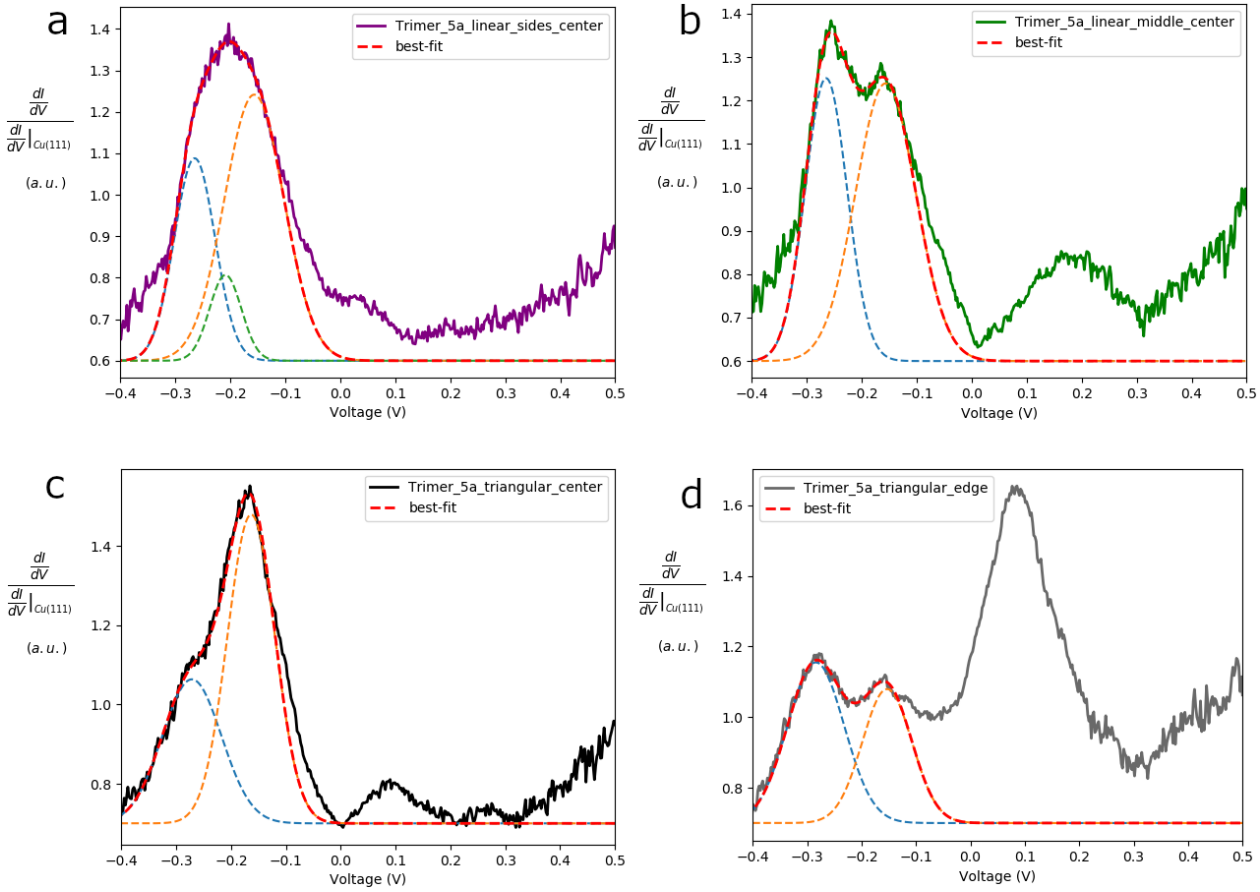

Figure 20: **a-d.** Normalized differential conductance spectra taken at the sites of corresponding color in figure 19.To characterize the energy splitting in the s orbitals, an amount of Gaussians equal to the amount of expected peaks was fitted such that their sum matched a best-fit for the spectra. The data was cropped to only the relevant peaks when obtaining the best-fit.

Table 4: Energy values obtained from the individual Gaussian fits on a linear and triangular trimer of edge type 5a blocked.

Type	E_+ ± 0.038 (eV)	E_- ± 0.055 (eV)	E_0 ± 0.029 (eV)
Linear	-0.265	-0.157	-0.209
Triangular	-0.278	-0.158	-

Table 5: Tight binding parameters obtained for a linear and triangular trimer of edge type 5a bocked.

Type	ϵ ± 0.021 (eV)	t ± 0.059 (eV)	s ± 0.059	t' ± 0.059 (eV)
Linear	-0.191	-0.049	0.409	0.019
Triangular	-0.212	-0.076	0.15	-

We determine the coupling in the triangular trimer in a similar way. Figure 20c shows the spectrum taken at the black positions in figure 19b. For a triangular trimer we calculated that the energy splits into two levels, the two fold degenerate level $E_+ = \frac{\epsilon - t}{1-s}$ and $E_- = \frac{\epsilon + 2t}{1+2s}$. The peak we see thus consists of two Gaussians. The sum was made to obtain a best fit and the centers of the original Gaussians were read off to obtain the energy levels $E_+ = -0.272$ eV and $E_- = -0.163$ eV. Figure 20d shows the spectrum taken at the grey positions in the scan of figure 19b where the p-like orbital is dominant. We do see two smaller peaks at the position where we expect the s orbital energies to be and by fitting two Gaussians to those we obtain $E_+ = -0.284$ eV and $E_- = -0.153$ eV. By averaging with the values of the black spectrum we obtain a better estimate for the true values, as shown in table 4.

Furthermore we note that the individual atoms in this triangular configuration would have an even lower on-site energy than the dimers and the linear trimer due to their larger surface area. We calculate the surface area to be 4.46 nm^2 by removing two more CO molecules which gives an on-site energy $\epsilon = -0.213$ eV. Now we can solve equations 21 and 22 to obtain the hopping parameter t and the orbital overlap s.

The obtained tight binding parameters for both the linear and the triangular trimer are shown in table 5. Uncertainties were estimated from the width of the Gaussians. For both trimers a molecular orbital diagram is shown in figure 21 showing which states correspond to which energy.

An important note to make on these trimers is the fact that both figure 20a and 20c show that the best fit is comprised of two Gaussians with a significantly different amplitude. Because we expect the confined surface states to all have the same scattering origin we would expect the Gaussians to have a similar width and amplitude.

For the linear trimer this deviation from expectation can be attributed to the fitting process. The acquired spectra can show some variation depending on the state of the STM tip and on the background. Even though the spectra are normalized with the Cu(111) background some deviations still remain. This gives the spectra an asymmetric shape which meant that the data had to be cropped to only the desired peaks to obtain a proper best fit. On the right side of the desired peak a small shoulder can be seen that should be neglected

in the fitting process. This meant that the data had to be cropped relatively far on the right side. This could have lead to the orange Gaussian being fitted a bit taller than it is actually supposed to be, which in turn lead to the green Gaussian being lower than that it is supposed to be. Since both the center and the width of the green Gaussian are in the range where they are expected to be we can argue that this is indeed the fit corresponding to the state with energy E_0.

For the triangular trimer a possible explanation lies in the fact that the orange dashed Gaussian from figure 20c corresponds to the degenerate energy level. If all states were to divide equally over the possible energy levels it would mean that twice as many states can sit at the degenerate energy level as the non degenerate one. This could explain why the local density of states is so much higher at the degenerate level.

The possible errors in this fitting process might explain the high value of the next nearest neighbor hopping t' as well. The tight binding parameters are quite sensitive to the on-site energy which also induces an error. Adding these errors together leads to a relatively high estimate for the uncertainties. A similar problem is illustrated in the MO diagram of the triangular trimer (21b), where the energy of the antibonding state of a dimer is higher in energy than the degenerate state of the trimer. Both values however are within the range of their uncertainties.

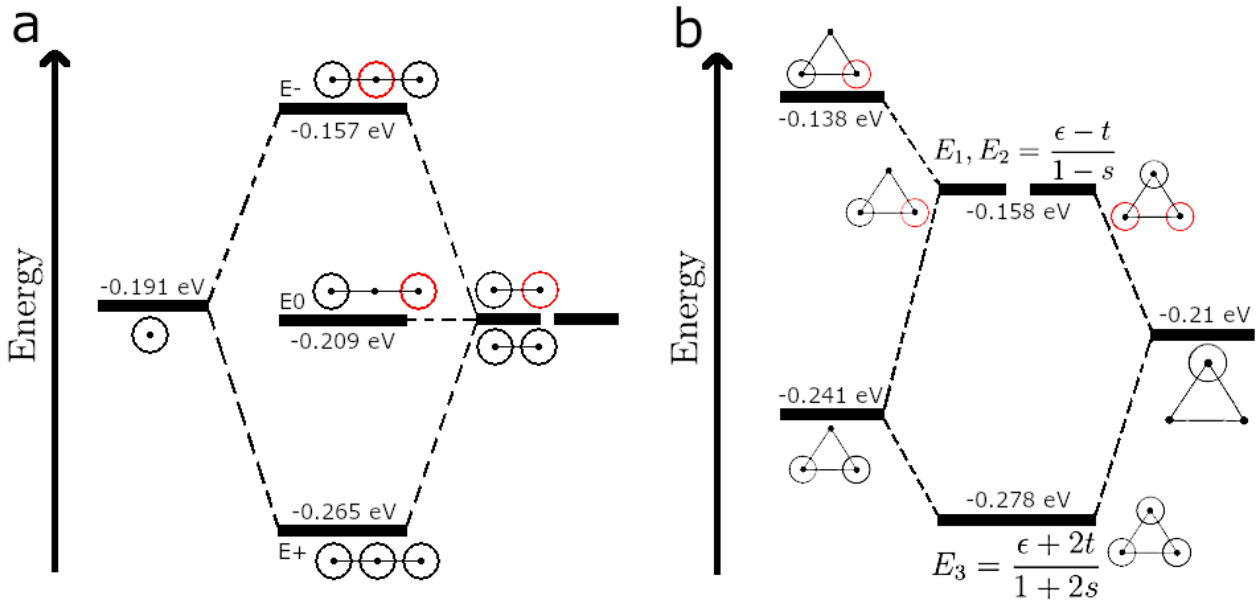

Figure 21: **a.** Molecular orbital diagram for the linear artificial trimer. **b.** Molecular orbital diagram for the triangular artificial trimer. In both figures the wave function localization on the atoms is indicated, black-black being a bonding combination, black-red antibonding.

4.2.6 P-like orbitals in a linear and a triangular trimer

To characterize the splitting in the p-like orbitals of the artificial trimers differential conductance spectra were acquired at the aquamarine, lime and gray sites indicated in figure 19. In figure 22a-c we present the way the p-orbitals in a linear trimer can bond. The spectra acquired on the linear trimer are shown in figure 22d. In the individual spectra however no

clear indication for energy splitting is found. This is likely due to the position where the spectra were taken. The spectra in lime were taken at a place where the antibonding state features a nodal plane. For this reason we only see a peak corresponding to the bonding state, indicated by the gray line through the spectrum. In the aquamarine spectrum we see the antibonding state most prominent. A small shoulder for the bonding state is also observed. The nonbonding state (22c) should be close to the same energy as the energy of the p-like orbitals in an individual atom (0.21 eV) but no indication for this is observed.

The energy corresponding to the bonding and antibonding orbital can be read off by fitting a Gaussian which yields the values $E_{bonding} = 0.03 \pm 0.012$ eV and $E_{antibonding} = 0.16 \pm 0.016$ eV for the linear trimer. The peak to peak difference is then 0.13 eV which is comparable to the difference between E_+ and E_- for the coupling of s orbitals in the linear trimer.

The spectrum taken on the triangular trimer is shown in figure 22 e. Here we see only one peak at $E = 0.09 \pm 0.015$ eV. A possible explanation for this is that the spectra were taken at a location where the other states featured a nodal plane. It is unclear to which state this energy corresponds. Because not all of the expected peaks were observed we were unable to calculate the tight binding parameters based on the coupling of the p like orbitals.

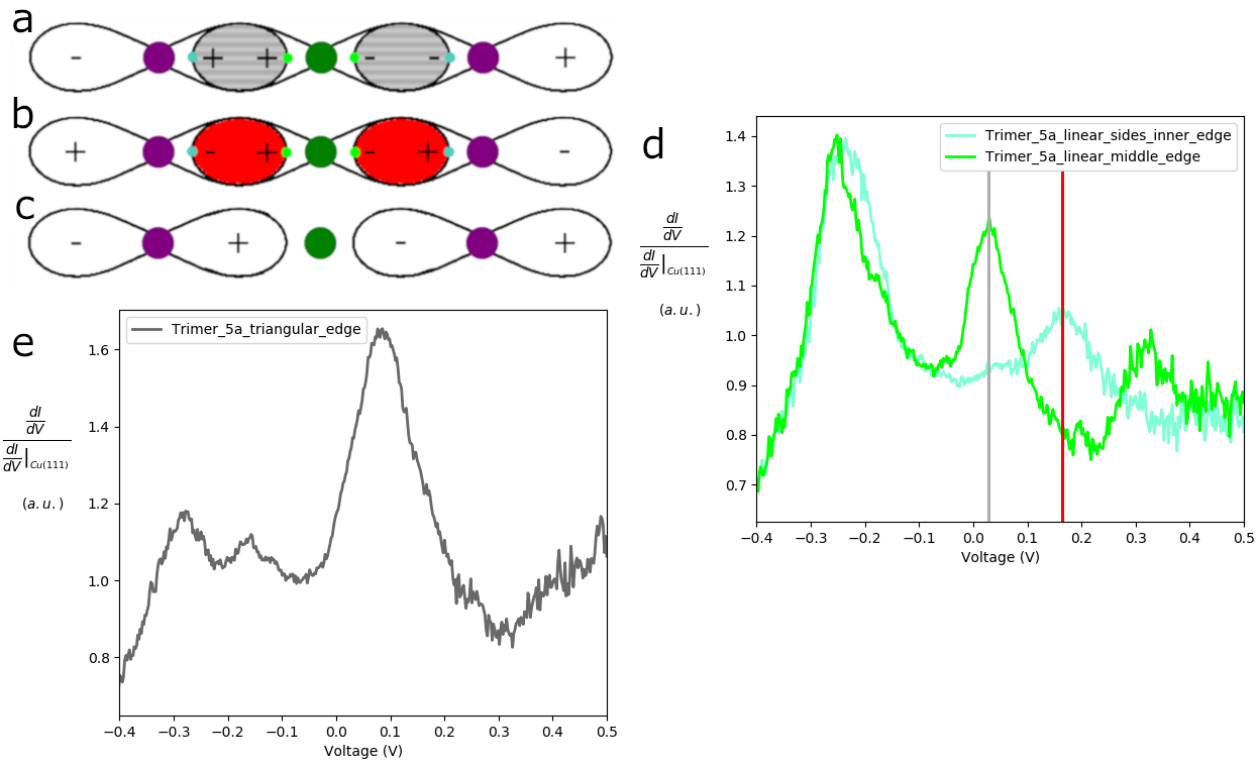

Figure 22: **Coupling of p-like orbitals in artificial trimers.** **a-c.** Schematic indication of how the p-orbitals of a linear trimer would bond. **a** shows the bonding state and **b** the antibonding state which features a nodal plane shown in red. **c** shows the nonbonding state. **d-e.** Normalized differential conductance spectra acquired on the linear and triangular trimer at the sites indicated by the same color in figure 19. For the linear trimer we show the peak corresponding to the bonding state with a gray line and the peak corresponding with the antibonding state with a red line.

5 Conclusions

The first goal of this research project was to build and characterize several configurations of artificial atoms. By varying individual atoms from a size of $2a$ to $6a$ and measuring the local density of states in an energy range of -0.6 to 0.5 eV it was confirmed that the on-site energy of these artificial atoms is lowered as their surface area is increased. The energy of the atoms follows a general particle-in-a-box like behavior, i.e. $E \propto \frac{1}{A}$, where A is the surface area.

On the larger atoms it was useful to add additional CO molecules along the edge of the atoms to disconnect the atom from its Cu(111) environment. This lead to a clearer peak in the LDOS spectrum. On the blocked $5a$ and $6a$ atoms spectra on the edge indicated the presence of a p-like orbital at energies of respectively $\epsilon_{p_{5a}} = 0.21$ eV and $\epsilon_{p_{6a}} = 0.17$ eV.

When two artificial atoms are coupled together their energy undergoes a splitting into a lower and higher energy state as is familiar from the tight binding approach. These dimers were built of the $4a$ and $5a$ blocked edge types and the barrier height between the two atoms was varied by altering the CO configuration in the middle. With a higher barrier the dimers showed less signs of splitting and with the lowest barrier there was a clear splitting from which the hopping parameters and orbital overlap could be determined. The $4a$ dimer showed hopping parameters $t = -0.121, t = -0.156$ eV and orbital overlap of $s = 0.659, s = 0.747$ for respectively a normal and a low scattering barrier. The $5a$ dimer has a hopping parameter of $t = -0.050$ and $t = -0.057$ eV and orbital overlap of 0.010 to 0.029.. Theoretical calculations showed similar LDOS spectra. From these theoretical calculations and experimental indications we also conclude that dimers with a high barrier behave as decoupled individual atoms.

Next three artificial atoms of the $5a$ blocked edge type were coupled together in a linear and triangular configuration. On the linear configuration the inner atom showed a splitting into two energy levels as was expected from tight binding. Using these two levels the third energy level could be determined from the differential conductance spectrum on the outer atoms. This splitting yielded a hopping parameter $t = -0.049$ eV, an orbital overlap $s = 0.409$ and a next nearest neighbor hopping parameter $t' = 0.019$ eV. The triangular configuration showed a splitting in accordance with tight binding as well, splitting into two states, one of which was degenerate. This lead to the hopping parameter $t = -0.076$ eV and orbital overlap $s = 0.15$. The linear trimer showed some indication of coupled p-like orbitals, having a bonding state at 0.03 eV and an antibonding state at 0.16 eV. The non bonding state could not be determined. The triangular trimer showed a p-like orbital at 0.09 eV but it could not be determined which state it corresponds to.

Secondly, the STM work function ϕ over a CO molecule was investigated. Because CO is generally imaged as a dip in the STM a higher work function was expected. Experiment however showed the work function above a CO molecule being -0.31 eV lower than the recorded work function on Cu(111). This was confirmed by a DFT calculation which showed a lowering of the work function in the same order of magnitude.

Furthermore when moving two CO molecules closer together their work functions do not change significantly until they are a distance $2a$ and a apart. At a distance $2a$ the work function shows no increase back to Cu(111) level in between the molecules but it is about 0.05 eV higher than the work function above a single CO molecule. At a distance a the work function increases by 0.21 eV above the Cu(111) level right in between the two molecules.

These characteristics of CO on Cu(111) are not fully understood. DFT calculations suggest that higher order terms in the tunneling current become important when measuring above a CO molecule[13], breaking down the general theoretical picture of tunnel current.

6 Outlook

The results discussed above yield a promising outlook for future experiments. The general behavior of these artificial atoms can function as a groundwork for larger lattices. We now know that blockers have some notable impact on the on-site energy and that from sizes $4a$ and onward they make the LDOS peak appear sharper.

Furthermore, we know that when coupling two or three atoms together the desired energy splittings are most prominent when the barrier between the atoms is lower than two normal coupled atoms, a feature that also finds its use in designing larger lattices. From these experiments we found that the hopping t was generally in the order -0.05 to -0.2 eV and the orbital overlap s in the order 0.01 to 0.8. These values can be useful when tuning tight binding models to experiments or to see if predictions made by theoretical models are experimentally accessible.

Besides larger lattices there are still many interesting properties to research on these smaller systems themselves. More research could be done on the energy of the bonding and anti bonding states in the dimers and trimers. It would be interesting to retake the spectra from the $4a$ dimer with a better tip to see if the theoretical model can experimentally be reproduced. Theoretical muffin tin and tight binding maps could be made and corroborated by experimental maps on both the dimers and trimers. This way one could find out if the LDOS is higher in the bonding or in the anti bonding state.

For the trimers we could take additional spectra to get a better picture of the splitting in the p-like orbitals. Aided by maps we could see which positions on the trimers feature a nodal point and which positions feature increased intensity. This can indicate some good positions to take the additional spectra.

Another consideration is the shape of these artificial atoms. By building square atoms one should be able to find a better fit to the square particle-in-a-box model when plotting on-site energy versus surface area. Comparing the fitted model to the theoretical model can then quantify the impact of CO molecules on the atom surface area. Since t and s were quite sensitive to the change in on-site energy an extended model of this would also benefit the results from the dimers and trimers.

From the work function profiles over the CO molecules we obtained more information about the general behavior of CO in STM experiments. Extra theoretical research could be done on additional terms in the formulas describing the tunnel current to see if these terms lead to a lowering of the work function above a CO molecule. Extra DFT calculations with a tip and an electric field present between the tip and sample could corroborate the experimental findings more. Recent research also shows that a metal tip can image CO molecules a protrusion rather than a dip at higher bias voltages [19]. It would thus be interesting to record more work function profiles over CO at different bias voltages.

7 Acknowledgements

Performing these experiments and writing this thesis would not have been possible without the help and guidance of several very valuable people to whom I'd like to extend my words of gratitude.

First of all I would like to thank *Saoirsé Freeney*, my daily supervisor, for guiding me through this project. You have taught me a lot about scanning tunneling microscopy and physics in general. Whenever disaster struck and samples dropped into the abyss you helped me stay positive and excited me for the research yet to come. Not only that but we've also had a lot of fun in the basement, from LN2 ice cream to accidentally falling asleep when playing relaxing brain waves for the STM. Every day has been of great pleasure to me and I am very thankful for this experience.

Next I would like to thank *Ingmar Swart* for providing me with the opportunity to do research in this group and for all the help with this project. We even went as far as filling the microscope with LHe on Christmas morning, for science!

I want to thank *Marlou Slot* for some insightful discussions about my results and *Jos Mulkens* for providing me with some chemical insight that I as a physicist was lacking. I want to thank *Jan Jurre Harsveld van der Veen* for his help and for prepping the tip to perfection.

A special word of thanks goes out to *Pierre Capiod* for doing the DFT calculations on the CO work function, providing me with some very valuable reference material. I want to thank *Jette van den Broeke* and *Mickey Bramer* from the Institute of Theoretical Physics here in Utrecht for the discussions and the theoretical calculations corroborating the spectra.

I want to thank *Noor ten Veen* for lending me her drawing tablet and teaching me how to use GIMP in order to make the images presented in this thesis as pretty as they are. Last but not least I want to thank Dr.*Peter Jacobse* for introducing me to the wonderful world of scanning tunneling microscopy (and the globglogabgalab) one and a half year ago.

Finally, I want to offer my sincere thanks to everybody in *Team Kelder* and *Condensed Matter and Interfaces* for the great atmosphere and for providing me with the opportunity to work with them. It has been a pleasure.

References

[1] Feynman, R. P. There's Plenty of Room at the Bottom. *CalTech Engineering and Science*. Volume **23:5**. February 1960. Transcript from `https://www.zyvex.com/nanotech/feynman.html`

[2] D. M. Eigler and E. K. Schweizer. Positioning single atoms with a scanning tunneling microscope. *Nature* **344**, 524-526. 05 april 1990.

[3] Moon, C. R. *et al.* Quantum phase extraction in isospectral electronic nanostructures. *Science* **319**, 782-787 (2008).

[4] Gomes, K. K. et al. Designer Dirac Fermions and topological phases in molecular graphene. *Nature*, **483**. 15 March 2012.

[5] Slot, M.R. et al. p-band engineering in artificial electronic lattices. *Physical Review X*. Accepted 28 November 2018.

[6] Kempkes, S. N., Slot, M. R. et al. Design and characterization of electrons in a fractal geometry. *Nature Physics*. 12 November 2018.

[7] Collins, L. C. et al. Imaging quasiperiodic electronic states in a synthetic Penrose tiling. *Nature communications* **8**, 15961 (2017).

[8] Kittel, C. 2005. *Introduction to Solid State Physics*. Eight edition. John Wiley & Sons, Inc.

[9] Julian Chen, C. 2008. *Introduction to Scanning Tunneling Microscopy*. Second edition. Oxford University Press.

[10] Swart, I. 2017. *Lecture notes 2017-2018 Solids & Solid Surfaces* Debye Institute for Nanomaterials Science, Utrecht University.

[11] Ashcroft, N. W. and Mermin, N. D. 1976. *Solid State Physics*. Nineteenth Indian Reprint 2017. Cornell University.

[12] Crommie, M.F., Lutz, C.P. and Eigler, D.M. Confinement of Electrons to Quantum Corrals on a Metal Surface. *Science Mag*, **262**, 08 October 1993.

[13] Gustafsson, A. and Paulsson, M. Scanning tunneling microscopy current from localized basis orbital density function theory. *Physical Review B* **93**, 115434. 24 March 2016.

[14] Scienta Omicron. Year unkown. *Fermi SPM - A cost effective concept for lower temperatures!*. From `https://www.scientaomicron.com/en/products/fermi-spm/instrument-concept`. Website consulted on 17-11-2018.

[15] Scienta Omicron. Year unknown. *LT STM - Ultimate SPM performance below 5K*. From `https://www.scientaomicron.com/en/products/low-temperature-spm/instrument-concept`. Website consulted on 13-12-2018.

[16] Stanford Research Systems. Date unknown. *About Lock-In Amplifiers*. From `https://www.thinksrs.com/downloads/pdfs/applicationnotes/AboutLIAs.pdf`. Website consulted on 22-12-2018.

[17] David, C. W. *The Particle in a Box (and in a Circular Box)*. 2006. Chemistry education materials. 12. From `http://digitalcommons.uconn.edu/chem_educ/12`. Consulted on 24-12-2018.

[18] Bramer, M. Quantum simulating electronic systems: elementary building blocks. *Scriptiearchief Universiteitsbibliotheek Utrecht*. 16-01-2019. `http://studenttheses.library.uu.nl/`.

[19] Zaum, C. and Morgenstern, K. Voltage dependent STM imaging of inorganic adsorbates. *Appl. Phys. Lett.* **113**, 031602 (2018).

A Sample preparation

Table 6: Overview of the preparation steps done on the Cu(111) sample on which the artificial atoms were built. The annealing temperature can be invoked from figure 23.

Procedure	Time (min)	Anneal voltage (V)	Anneal current (A)	Pressure ($\times 10^{-6}$) (mbar)
Sputter	20			3.9
Anneal	7	19.99	1.42	
Sputter	20			4.0
Anneal	7	19.99	1.42	
Sputter	20			3.8
Anneal	7	19.99	1.42	
Sputter	20			3.7
Anneal	7	19.99	1.42	
Sputter	20			3.7
Anneal	7	19.99	1.43	
Sputter	20			3.7
Anneal	7	19.99	1.44	
Sputter	20			3.7
Anneal	7	19.99	1.42	
Sputter	30			3.6
Anneal	7	19.99	1.41	
Sputter	20			3.6
Anneal	7	19.99	1.40	

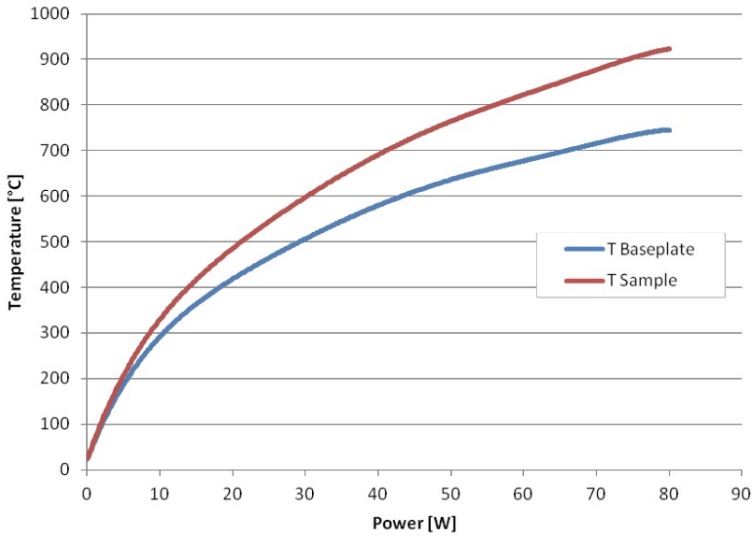

Figure 23: Temperature curve for the heater arm in the preparation chamber of the LT setup. Image taken from Scienta Omicron: *LT STM system upgrade*. 26 October 2017.

B Artificial atoms

Table 7: Overview of all artificial atoms/structures that have been built and analyzed by measuring the differential conductance and fitting Gaussians to the relevant peaks.

Type	Design	Scan (0.100 V & 30 pA)	Spectrum
Hexagonal Atom $2a$	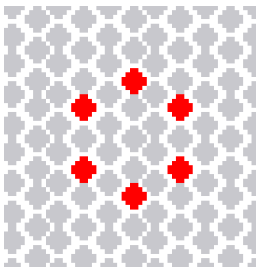	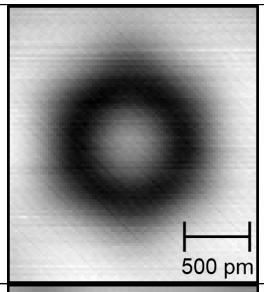	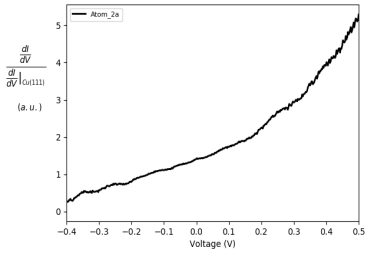
Hexagonal Atom $3a$	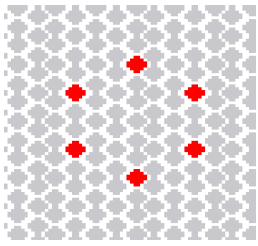	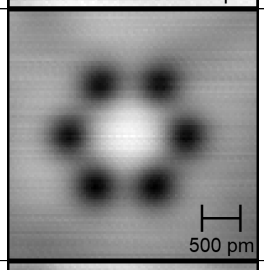	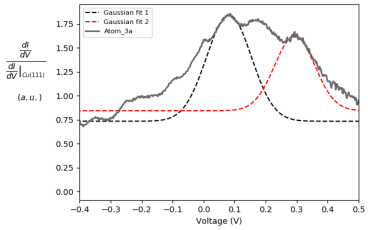
Hexagonal Atom $4a$	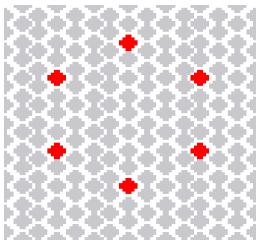	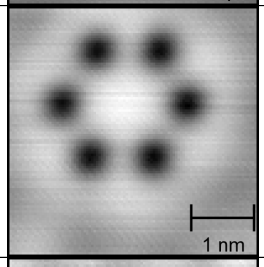	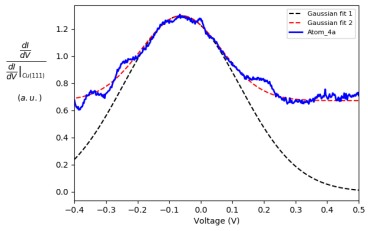
Hexagonal Atom $4a$ Blocked	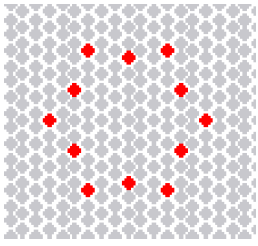	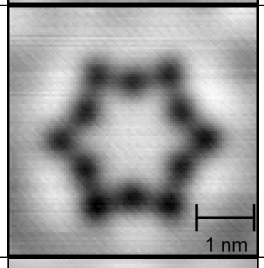	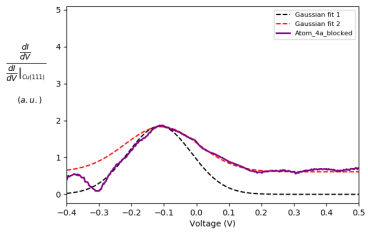
Hexagonal Atom $5a$	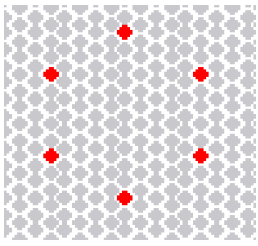	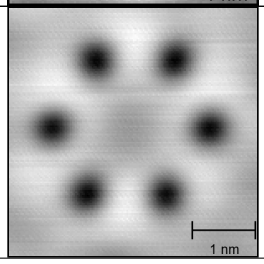	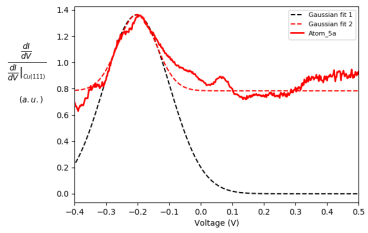

Hexagonal Atom $5a$ Blocked	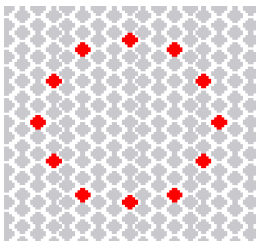	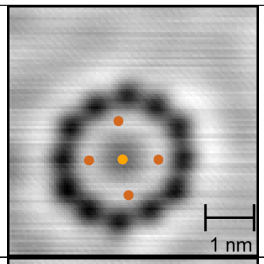	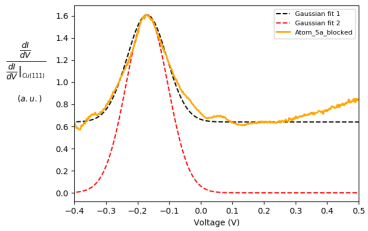
Hexagonal Atom $5a$ Blocked	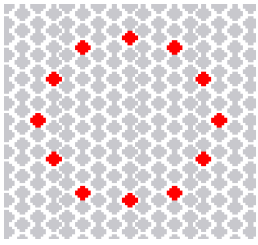	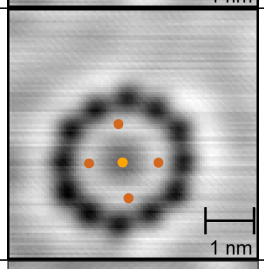	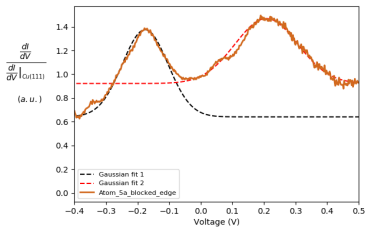
Hexagonal Atom $6a$ Blocked	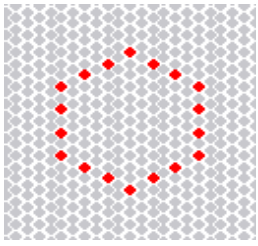	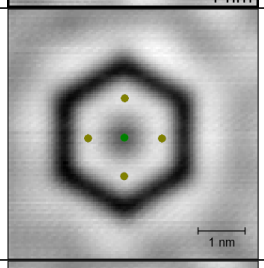	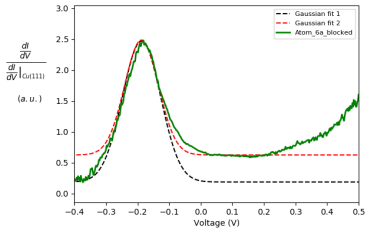
Hexagonal Atom $6a$ Blocked	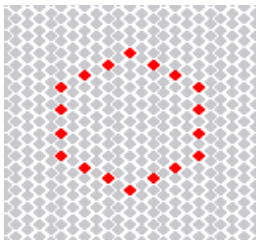	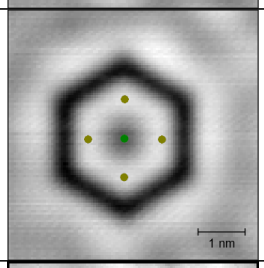	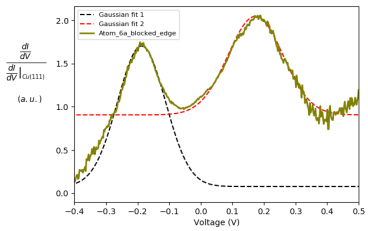
Hexagonal Dimer $4a$ Normal Barrier	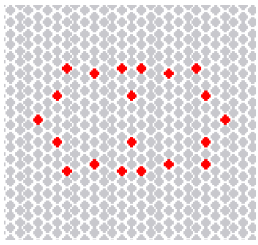	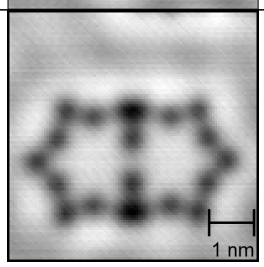	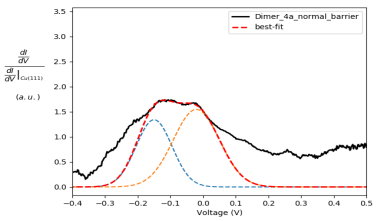
Hexagonal Dimer $4a$ lower Barrier	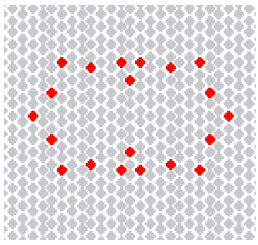	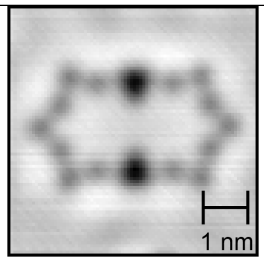	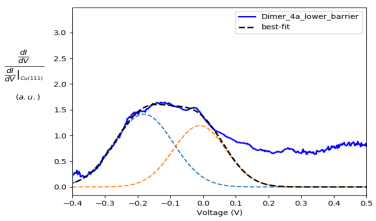

Hexagonal Dimer $4a$ Higher Barrier	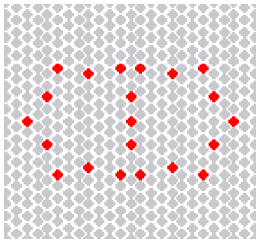	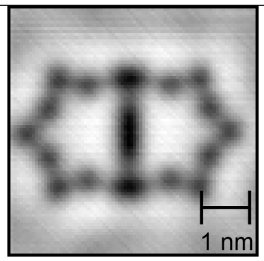	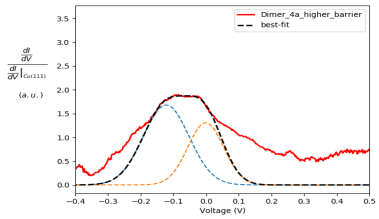
Hexagonal Dimer $5a$ Normal Barrier	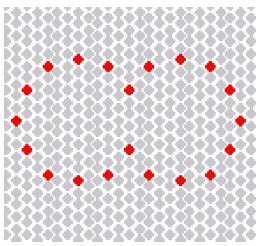	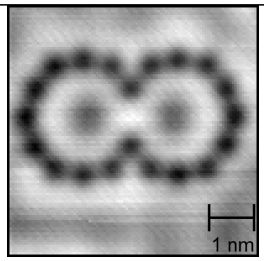	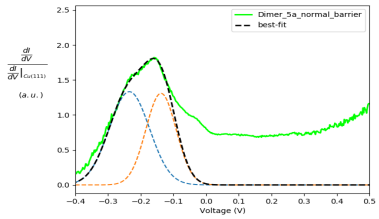
Hexagonal Dimer $5a$ Lower Barrier	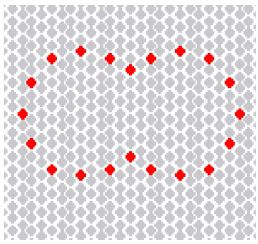	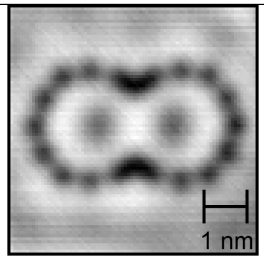	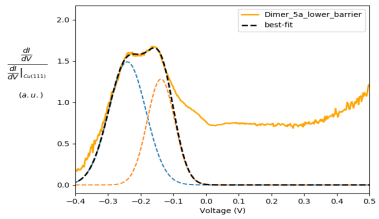
Hexagonal Dimer $5a$ Higher Barrier	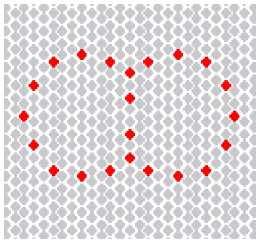	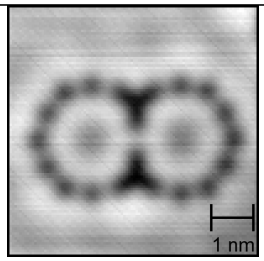	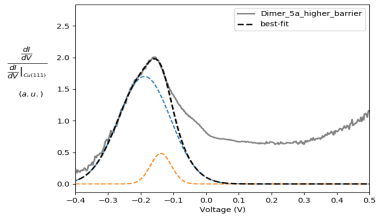
Hexagonal Trimer $5a$ Linear side outer edge	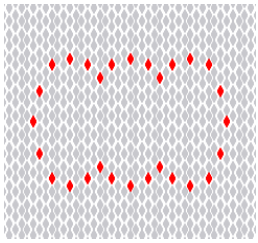	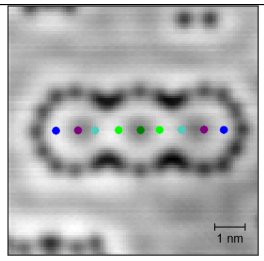	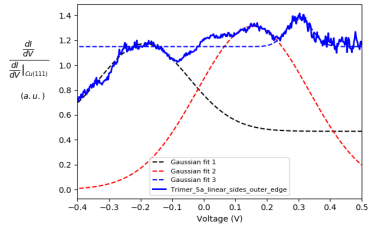
Hexagonal Trimer $5a$ Linear side center	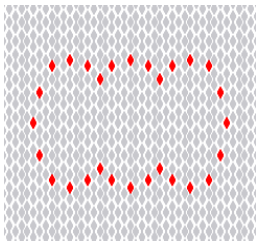	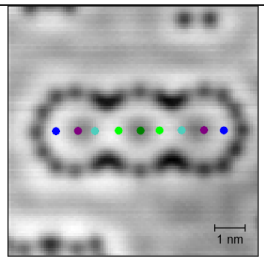	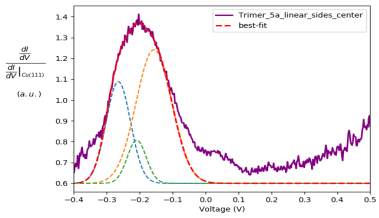

Hexagonal Trimer $5a$ Linear side inner edge	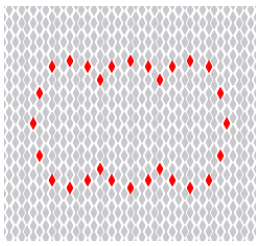	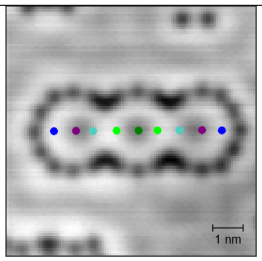	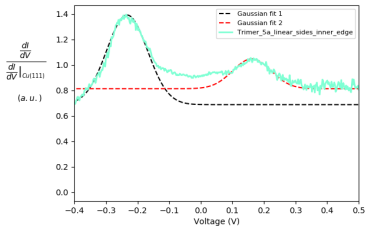
Hexagonal Trimer $5a$ Linear middle edge	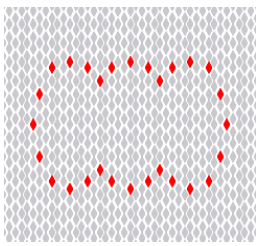	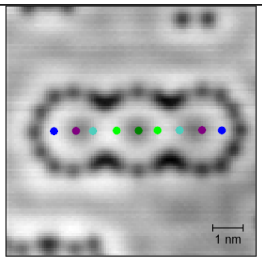	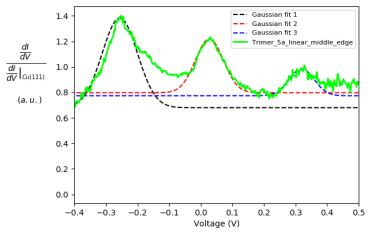
Hexagonal Trimer $5a$ Linear middle center	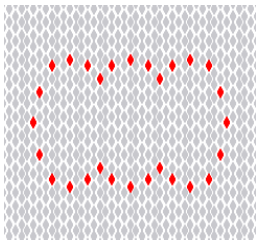	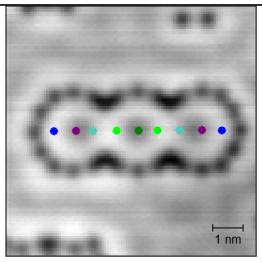	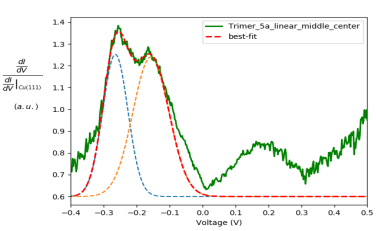
Hexagonal Trimer 5a tirangular center	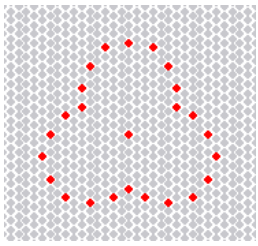	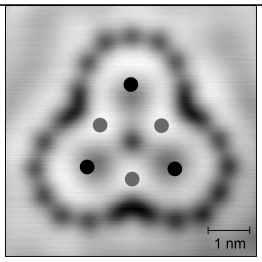	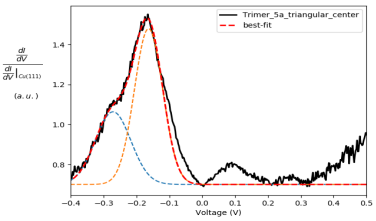
Hexagonal Trimer 5a triangular edge